THESIS

MODELING LISEGANG PATTERN FORMATION IN THE COUNTERDIFFUSION OF

AMMONIA AND HYDROGEN CHLORIDE

Submitted by

Leah D. Gibson

Department of Mathematics

ABSTRACT

MODELING LISEGANG PATTERN FORMATION IN THE COUNTERDIFFUSION OF

AMMONIA AND HYDROGEN CHLORIDE

Liesegang patterns form as a result of chemical reaction and diffusion. To this day, there is no agreed-upon single method of mathematically modeling Liesegang pattern formation. The goal of this paper is to explore a variety of models for Liesegang pattern formation specifically applied to the counterdiffusion of vapor-phase ammonia (NH_3) and hydrochloric acid (HCl), whose product, solid ammonium chloride, forms these Liesegang patterns. The modeling here focuses on prenucleation models, where it is believed that Liesegang patterns form during the nucleation process. We develop multiple theoretical models for the nucleation and growth of $HCl + NH_3$. We implement a new "kinetic" approach to modeling nucleation and growth that tracks particle sizes. Work still remains to numerically simulate some of the models and compare them to observational data to determine the best modeling approach to Liesegang pattern formation applied to the counterdiffusion of NH_3 and HCl.

TABLE OF CONTENTS

Chapter 1

Liesegang Patterns: Experiments & Theory

1.1   Introduction

Liesegang patterns, also known as periodic precipitation, occur across a wide variety of chemical reactions, time scales, and spatial scales. They are characterized by patterns of rings or bands that often form as a result of a precipitation reaction [18]. See Figure 1.1 for an example of Liesegang rings produced by vapor-form ammonia and hydrochloric acid undergoing a series of reactions that result in solid ammonium chloride. A variety of chemical reactions form Liesegang patterns in a labratory setting [5, 28]. These reactions happen relatively quickly and on a small spatial scale. However, Liesegang banding also appears naturally in rocks such as rhyolite and sandstone [21]. Perhaps one of the most well known natural landmarks with Liesegang patterns is The Wave in Arizona, made of Navajo Jurassic sandstone.

Liesegang pattern formation is of interest because there is no single agreed-upon model or theory of how exactly these unique patterns form [18]. The aim of this paper is to explore various theoretical models of Liesegang pattern formation and then apply them to the counterdiffusion reaction of hydrogen chloride (HCl) and ammonia (NH_3). The counterdiffusion of HCl and NH_3 is a reaction-diffusion system where the diffusion of both gases into a long and narrow tube results in the formation of solid ammonium chloride ($NH_4Cl_{(s)}$) which forms a Liesegang pattern under the right conditions. This formation of solid is called nucleation which is formally defined as the formation of a new phase from one or more existing phases.
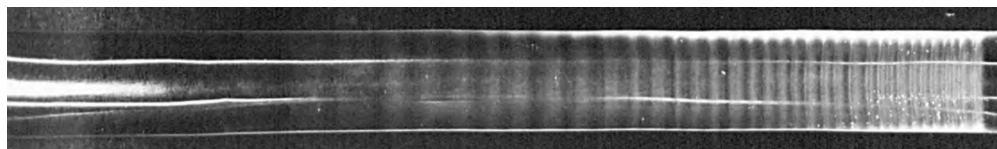

Figure 1.1: The formation of Liesegang bands produced by the counterdiffusion of hydrogen chloride gas (HCl) and ammonia gas (NH_3). Photo from Swaran Singh [23].

Acid-base reactions such as this also have applications outside of Liesegang pattern formation. Other acids such as sulfuric acid and nitric acid react with ammonia gas in the atmosphere, leading to particle formation and growth that can impact the radiative balance of the atmosphere [9]. Precipitation reactions similar to the ones discussed here can also be applied to these atmospheric acid-base reactions.

This paper is broken into two chapters. The first chapter provides a general overview of Liesegang pattern formation theories in Section 1.2 and introduces the counterdiffusion experiment in Section 1.3. The second chapter applies these foundational models to the counterdiffusion experiment. Section 2.1 applies a nucleation and growth model to the counterdiffusion reaction using classical nucleation theory. The model in this section is also simulated numerically and compared to observational data from [23]. Section 2.2 provides a broad introduction to coagulation, the action of particles growing by sticking together. The following two sections then use coagulation in their models. Section 2.3 uses coagulation as a means of developing a kinetic model of nucleation where the growth of clusters of gas, called i-mers, is the mechanism that drives nucleation. Section 2.4 also uses coagulation to model the growth of nucleated particles. Section 2.5 then builds on the previous two sections, combining them to form a sol-coagulation model that includes a separate agglomeration (or coagulation) and precipitation step as well as nucleation and growth step. The final part of this paper outlines the future work and goals for each model.

1.2   Modeling Liesegang Pattern Formation

Liesegang patterns were first observed and documented by by German chemist Raphael E. Liesegang [15]. The canonical system used to create Liesegang patterns (also known as periodic precipitation) involves two reagents placed in a gel medium. However, as it's seen in the counterfiffusion of ammonia and hydrogen chloride, it is possible to see Liesegang patterns produced outside of this gel setting. The commonality between the two is the reaction of two reagents which are transported via diffusion.

As a testament to the difficulty of Liesegang modeling, there is still no standard model for Liesegang pattern formation. The foundational models are broken into two main categories, prenucleation models and postnucleation models [18]. Both models begin with diffusion of two species A and B which then react to form some product C. In the prenucleation models, the overarching assumption is that pattern formation occurs during the nucleation process. In regions where the concentration of C exceeds a given supersaturation threshold, nucleation occurs and the concentration of C is depleted below the supersaturation level, ceasing the formation of solid. Driven by diffusion the reaction front where the two reactants meet moves, and the concentration of C again builds until nucleation occurs again. This process repeats itself over and over, forming Liesegang bands. Under the postnucleation model, band formation does not occur in the nucleation step. Instead, it is assumed that precipitate is constantly deposited and bands form as a result of thermodynamic instability and competitive particle growth.

It is important to note that some of the assumptions made in these models are not completely physical and ignore some likely processes that happen throughout the reaction. However, any model makes simplifying assumptions at the expense of complete accuracy. The Liesegang models outlined in this section are older and more basic, but the hope is that these models - while lacking in some ways - still help build an understanding of some of the mechanics and theories behind Liesegang pattern formation. Section 1.3.1 also gives an example of an alternative approach to modeling counterdiffusion reactions, although these these theories are not pursed further in this paper.

The following subsections describe the different prenucleation and postnucleation models as outlined by [18]. The theory and models outlined here can apply to any periodic precipitation reaction, so each model is discussed in general terms. Note that it is also possible to combine the two theories as was done by Chacron and L'Heureux [1]. However here, for the sake of outlining the basic models, they will be discussed separately.

1.2.1 Prenucleation Liesegang Models

The key difference between prenucleation and postnucleation models is *when* pattern formation is believed to happen. Prenucleation models assume that pattern formation occurs in tandem with nucleation itself. There are three main models that fall under prenucleation models: the supersaturation model, the nucleation and growth model, and the sol-coagulation model. Each grows more sophisticated to address concerns of its predecessor. Outlining each model also provides a historical timeline of evolution of periodic precipitation modelling, so it is important to note that many of the models used now are more complex than models here, but are still fundamentally based on the theory developed here.

The Supersaturation Model

The simplest description of Liesegang pattern formation using a prenucleation model combines gas reactants A and B to form precipitate C.

$$A_{(g)} + B_{(g)} \xrightarrow{k} C_{(s)} \tag{1.1}$$

This basic model is called the supersaturation model and was first introduced by German chemist Wilhelm Ostwald [16]. In the supersaturation model, nucleation is triggered when the concentration of the product AB exceed a certain supersaturation threshold, c_{SS}. Nucleation ceases when the concentration of product drops below the supersaturation threshold. Supersaturation occurs when the vapor pressure of the gas exceeds the equilibrium pressure of the gas. Note that under this model, it is impossible for solid to form between bands since $f(A, B)$ is zero when the concentration product is less than c_{SS}. This reaction-diffusion system is modeled:

$$\frac{\partial A}{\partial t} = D_A \frac{\partial^2 A}{\partial x^2} - kf(A, B) \tag{1.2}$$

$$\frac{\partial B}{\partial t} = D_B \frac{\partial^2 B}{\partial x^2} - kf(A, B) \tag{1.3}$$

$$\frac{\partial C}{\partial t} = kf(A, B) \tag{1.4}$$

where $f(A, B)$ is the nucleation function, D_A and D_B are the diffusion coefficients of the reactants, and k is a rate constant to account for how quickly A and B form C. To align with other supersaturation models, we assume that the precipitate is large and immobile [1]. Thus there is no diffusion coefficient for the precipitate.

There are numerous models for the nucleation function. The simplest is a step function in which $f(A, B)$ is nonzero if the product AB is bigger than the supersaturation threshold and zero otherwise. However, some experiments show that a detectable amount of precipitate – even if they are not visible to the naked eye – forms between bands. To account for this, a model by G.T. Dee adds an intermediary step in the supersaturation model [3]. This leads to the next model.

Nucleation and Growth Model

The nucleation and growth model developed by G.T. Dee [3] differentiates between the formation of product the the nucleation of the product by assuming that the reactants form a product in gas form before it nucleates. This step allows for more control in how nucleation occurs.

$$A_{(g)} + B_{(g)} \xrightarrow{k_1} C_{(g)} \tag{1.5}$$

$$C_{(g)} \xrightarrow{k_2} P_{(s)} \tag{1.6}$$

In Dee's nucleation and growth model, the product C forms by the reaction of A and B, and solid P forms from the nucleation of C using the same supersaturation assumptions as before. The nucleation and growth model is written in the following way:

$$\frac{\partial A}{\partial t} = D_A \frac{\partial^2 A}{\partial x^2} - k_1 AB \tag{1.7}$$

$$\frac{\partial B}{\partial t} = D_B \frac{\partial^2 B}{\partial x^2} - k_1 AB \tag{1.8}$$

$$\frac{\partial C}{\partial t} = D_C \frac{\partial^2 A}{\partial x^2} + k_1 AB - K_2 f(C, P) \tag{1.9}$$

$$\frac{\partial P}{\partial t} = k_2 f(C, P) \tag{1.10}$$

The reaction rate, k_2, models the rate at which gas precipitates. Note that the precipitate does not diffuse, so the only way for detectable amounts of precipitate to form between bands is if the nucleation function $f(C, P)$ is non-zero but small between bands. Depending on the function used, this is possible.

The following nucleation function proposed by Keller and Rubinow takes the basic piecewise function described previously and sophisticates it [13], but does not allow for precipitate formation between bands. Just like in the supersaturation model, Keller and Rubinow assume that C precipitates only when its concentration exceeds a supersaturation concentration threshold c_{SS}. Now, precipitation continues until the concentration of C drops below a saturation concentration $c_S < c_{SS}$ (when the vapor pressure of the gas equals the equilibrium pressure of the gas). The Keller-Rubinow nucleation function [13] is thus given by

$$f(C, P) = \begin{cases} 0 & C < c_{SS} \text{ and } P = 0 \\ C - c_S & C \geq c_{SS} \text{ or } P > 0 \end{cases} \tag{1.11}$$

Notice that in the Keller-Rubinow model, precipitation occurs two ways: either the concentration of C exceeds the supersaturation threshold, or precipitate is already present in the system. Thompson et al. [27] connect these two scenarios to the concepts of a homogeneous and heterogeneous nucleation threshold. Homogeneous nucleation refers to nucleation occurring without the aid of a different phase ($C > c_{ss}$). Homogeneous nucleation is difficult and requires a much higher supersaturation threshold. Heterogeneous nucleation occurs when nucleation is aided by preexisting particles; like the presence of precipitate [27]. Heterogeneous nucleation is significantly easier to achieve. Note that in some definitions, the formation of precipitate on already existing precipitate is not considered heterogeneous nucleation. However, to remain consistent with the foundational work from Thompson et al. [26, 27] on which this paper is based, we will use their definition of a heterogeneous nucleation threshold which includes nucleation on already formed precipitate.

Thompson et al. write the Keller-Rubinow model as:

$$f(C, P) = \begin{cases} 0 & C < c_*(P) \\ C - c_s & C \geq c_*(P) \end{cases}$$

where

$$c_*(P) = \begin{cases} c_s > 0 & P > 0 \\ c_{ss} > c_s & P = 0 \end{cases} \tag{1.12}$$

where c_{ss} acts as a homogeneous nucleation threshold and c_s acts as a heterogeneous nucleation threshold. In this model, it is assumed that heterogeneous nucleation is catalyzed by already existing precipitate in the system [27]. For a more in depth exploration of the Keller-Rubinow model, see [6, 7].

A discontinuous function such as the Keller-Rubinow function poses numerical difficulties and often produces Liesegang bands that are a single grid point wide [6]. As a result, there are a number of alternative functions posed to replace the Keller-Rubinow model but still create the desired results. A number of these are discussed in [8]. A smoothed version of the Keller-Rubinow model is also presented and numerically simulated in Section 2.1.

Sol-coagulation Model

Equation 1.6 of the nucleation and growth model groups many processes into a single step. This step includes an aggregation and precipitation step as well as a nucleation and growth step all as a single process. Aggregation (which will be used interchangeably with "coagulation" in reference to gas molecules here) is the process of particles sticking together to form larger clusters or molecules. Precipitation is the process of forming a solid from a supersaturated gas. As stated previously, nucleation is the formation of a new phase - so it is essentially the same as precipitation in the

7

context here. Growth then refers to how nucleated particles increase in size. The sol-coagulation model, developed by Dhar [4] differentiates these processes by adding another intermediary step.

$$A_{(g)} + B_{(g)} \rightarrow C_{(g)} \tag{1.13}$$

$$C_{(g)} \rightarrow C_{(s)} \tag{1.14}$$

$$C_{(s)} \rightarrow P_{(s)} \tag{1.15}$$

Equation 1.14 accounts for the aggregation and precipitation of gas particles while Equation 1.15 then models the nucleation and growth of the precipitate. Thus $C_{(s)}$ should be though of as small, freshly nucleated particles, whereas $P_{(s)}$ are larger particles that have grown after nucleating. The purpose of separating these processes is to differentiate between the mechanics that cause nucleation and the mechanics that cause nucleated material to grow in size. Section 2.3 gives an example of a model for the aggregation of particles using a kinetic theory of gases. Section 2.4 then discusses a model for the growth of precipitate. Section 2.5 combines these models into a sol-coagulation model.

1.2.2 Postnucleation Liesegang Models

Postnucleation models are characterized by pattern formation happening *after* nucleation. They assume that nucleation occurs homogeneously throughout the space and precipitation bands then form after nucleation via competitive particle growth. One such postnucleation theory is Ostwald ripening [19]. Under this theory, larger particles grow at the expense of smaller particles. This is because the curvature of smaller particles makes them more soluble, and thus more likely to be "eaten" by the larger particles [17]. This phenomena is also known as the Kelvin effect and the Kelvin equation shows that smaller particles are more soluble than large ones [25]. This process of larger particles growing at the expense of smaller particles causes Liesegang rings, hence characterizing it has a postnucleation model.

No explicit postnucleation models are discussed here because the remainder of the paper explores prenucleation models. However, some people believe that the sol-coagulation model from Section 1.2.1 could be characterized as a postnucleation model depending on how the nucleation and growth step is modeled [18]. This is because the model does not specify whether pattern formation should occur in the aggregation and precipitation step (Equation 1.14) – which would characterize it as a prenucleation model – or in the nucleation and growth step (Equation 1.15) – which would categorize it as a postnucleation model since pattern formation occurs after nucleation. For example, if the nucleation and growth step in Equation 1.15 were to include a process such as Ostwald ripening, we would likely see pattern formation occur after nucleation.

1.3   The Counterdiffusion Experiment

This paper primarily focuses on developing theoretical models for Liesegang pattern formation. Results of the models can be compared to already existing experimental results from the PhD thesis of Swaran Singh [23]. Thus the models aims to mimic the conditions as outlined in Singh's counterdiffusion experiments. A brief set up of the experiment is given here and a more in depth description can be found in Singh's thesis.

The experiments use a narrow glass tube 0.80 cm in diameter and 67 cm long fitted between two gas reservoirs. One reservoir contains hydrogen chloride and the other ammonia gas. The tube itself is initially filled with either pure nitrogen gas or nitrogen gas saturated with some level of water vapor in order to observe the effects of moisture on the diffusion and ring formation process. In the counterdiffusion experiment, both gases diffuse simultaneously into the tube from the ends. The location when the two gases meet and react is called the reaction front. During the experiment, the reaction front travels monotonically down the tube from its starting location. The direction that the front travels is determined by the initial concentrations of reactants. More specifics of the front are explained in Section 2.1.2. As times goes on, the diffusion-driven reaction front travels down the tube, leaving the product of HCl and NH_3, nucleated ammonium chloride ($NH_3Cl_{(s)}$) in its wake. Nothing is seen in the tube until $NH_4Cl_{(s)}$ forms and grows. The precipitate appears as
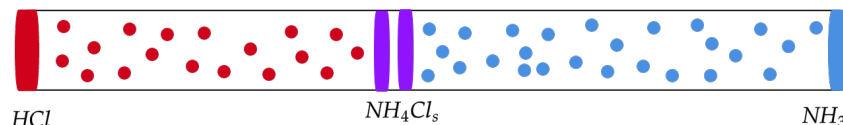
Figure 1.2: The basic set up of the $HCl + NH_3$ counterdiffusion experiment.

white powder coating the tube in the nucleation location. These rings of $NH_4Cl_{(s)}$ are fixed in place once deposited because many of the particles stick to the glass tube. This counterdiffusion experiment is specifically unique because of the way in which $NH_4Cl_{(s)}$ is deposited. Under certain moisture levels and reactant concentrations, $NH_4Cl_{(s)}$ forms Liesegang rings. See Figure 1.2 for a visual of the basic counterdiffusion experiment with Liesegang ring formation as described above. Section 1.2 further discusses Liesegang rings and the various theories and methods of modeling this phenomena.
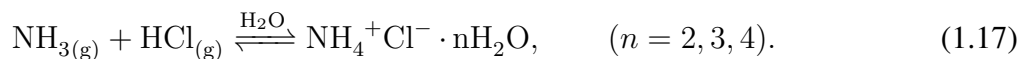
Water plays a role in the formation of Liesegang rings in the counterdiffusion experiment. Singh showed that the Liesegang rings are formed only when moisture is present in the tube. If there is no moisture in the system, there is continuous precipitation instead of bands of periodic precipitation [23]. Singh also found that once there is sufficient moisture in the tube to cause Liesegang band formation, the water has no noticeable effect on the particle size distribution in rings [23]. The models below do not specifically take into account the existence of water, and it is instead assumed that the parameters used indirectly assume the existence of sufficient water vapor for pattern formation. Thus the hope is that all of the models below produce Liesegang banding. The model of ammonium chloride formation and nucleation in the following section (1.3.1) highlights the role that water plays in the reaction.

1.3.1 Nucleation via Ion Transfer
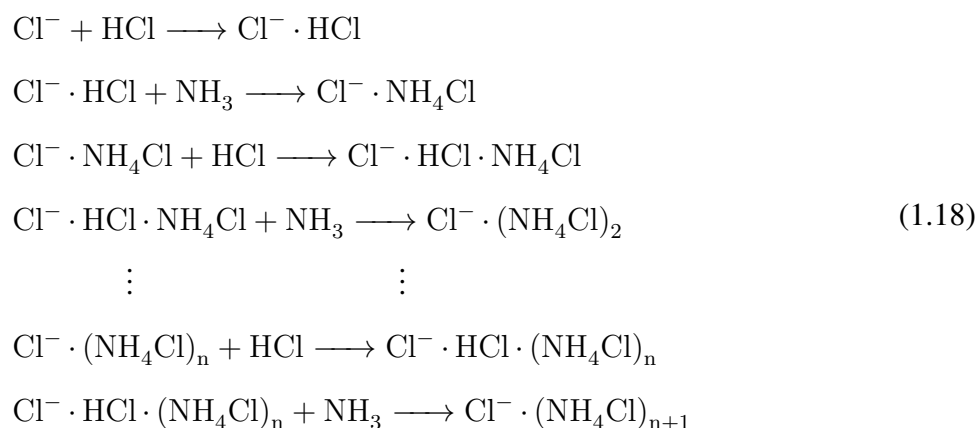
This section offers a brief alternative mechanism and theory for the $HCl + NH_3$ reaction based on work from Thompson et al. [26]. Refer to their work for more details. We begin with the overall process

$$NH_{3(g)} + HCl_{(g)} \longrightarrow NH_4Cl_{(s)}. \tag{1.16}$$
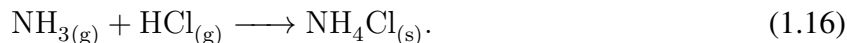
which mirrors the supersaturation model in Section 1.2.1. However, the next assumptions stray from the over-simplified assumptions of the supersaturation model. The next step is a water-catalyzed proton transfer, where it becomes obvious that water plays an important role in the reaction if it is present

$$\text{NH}_{3(g)} + \text{HCl}_{(g)} \xrightleftharpoons{\text{H}_2\text{O}} \text{NH}_4{}^+\text{Cl}^- \cdot \text{nH}_2\text{O}, \qquad (n = 2, 3, 4). \tag{1.17}$$

This transfer produces an ammonium ion NH_4^+ and a chlorine ion Cl^-. Thompson et al. speculate that this previous step is different under anhydrous conditions. The Cl^- ions can act as catalyst to induce nucleation which is then followed by step-wise addition of HCl and NH_3 monomers:

$$
\begin{aligned}
\text{Cl}^- + \text{HCl} &\longrightarrow \text{Cl}^- \cdot \text{HCl} \\
\text{Cl}^- \cdot \text{HCl} + \text{NH}_3 &\longrightarrow \text{Cl}^- \cdot \text{NH}_4\text{Cl} \\
\text{Cl}^- \cdot \text{NH}_4\text{Cl} + \text{HCl} &\longrightarrow \text{Cl}^- \cdot \text{HCl} \cdot \text{NH}_4\text{Cl} \\
\text{Cl}^- \cdot \text{HCl} \cdot \text{NH}_4\text{Cl} + \text{NH}_3 &\longrightarrow \text{Cl}^- \cdot (\text{NH}_4\text{Cl})_2 \\
\vdots \qquad\qquad & \qquad\qquad \vdots \\
\text{Cl}^- \cdot (\text{NH}_4\text{Cl})_n + \text{HCl} &\longrightarrow \text{Cl}^- \cdot \text{HCl} \cdot (\text{NH}_4\text{Cl})_n \\
\text{Cl}^- \cdot \text{HCl} \cdot (\text{NH}_4\text{Cl})_n + \text{NH}_3 &\longrightarrow \text{Cl}^- \cdot (\text{NH}_4\text{Cl})_{n+1}
\end{aligned}
\tag{1.18}
$$

As opposed to the nucleation theories in Section 1.2, this theory does not require the formation of $\text{NH}_4\text{Cl}_{(g)}$ or nucleation thresholds. Instead, this theory assumes that nucleation occurs and precipitate grows by the addition of ions. While this theory is not modeled or further explored in this paper, it could be in the future to test its ability to produce Liesegang rings and explicitly incorporate water in the reaction.

Now that the basic models of Liesegang pattern formation have been outlined and the set up of the counterdiffusion experiment explained, Chapter 2 applies versions of these models to the counterdiffusion experiment.

Chapter 2

Modeling the Counterdiffusion Experiment

In this chapter, we now apply versions the previously discussed models to the counterdiffusion of HCl and NH_3. Some of the models are compared against data and observations from Singh to test the accuracy of the model.
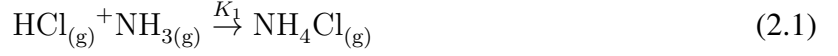
2.1 Classical Nucleation Theory

This section uses a nucleation and growth model to model Liesegang pattern formation for the $HCl + NH_3$ system. The work here is based on foundation work from Hashmi et al. [11].

2.1.1 Classical Nucleation and Growth Model

Classical nucleation theory follows a prenucleation theory. Thus it is assumed that nucleation happens as a result of supersaturated gas; that is the vapor pressure of the gas exceeds the equilibrium pressure of the gas. This ratio is known as the supersaturation ratio, c_{ss}. For nucleation to occur, c_{ss} must be significantly greater than 1. As seen in the Keller-Rubinow nucleation function from Equation 1.11 and its version from Equation 1.12, there are two main types of nucleation: homogeneous and heterogeneous nucleation. Corresponding to homogeneous and heterogeneous nucleation are homogeneous and heterogeneous nucleation thresholds. These values correspond to the concentration of $NH_4Cl_{(g)}$ required to nucleate under different conditions. A homogeneous nucleation threshold is relevant when nucleation is not aided by already existing solid. The heterogeneous nucleation threshold is applicable when nucleation is aided by solid such nucleated precipitate or other contaminates in the system like dust [27].

In the following model, we assume the system to be free of contaminates. Thus heterogeneous nucleation only occurs when $NH_4l_{(s)}$ is already present at that location in the tube. In the model, the homogeneous nucleation threshold is 0.02 mmHg and the heterogeneous nucleation threshold is 0.002 mmHg, based on values used by Thompson et al. [27].

Many models for the counterdiffusion of ammonia and hydrogen chloride use classical nucleation and growth models such as the basic models used in [6, 7, 12, 27]. Here, we explore a nucleation and growth model specifically based on the work of Hashmi et al. [11]. Applying the nucleation and growth model outlined in Section 1.2.1 to this counterdiffusion system yields

$$\text{HCl}_{(g)} + \text{NH}_{3(g)} \xrightarrow{K_1} \text{NH}_4\text{Cl}_{(g)} \tag{2.1}$$

$$\text{NH}_4\text{Cl}_{(g)} \xrightarrow{K_2} \text{NH}_4\text{Cl}_{(s)} \tag{2.2}$$

Referring back to Figure 1.2, let HCl vapor enter on the left end of a tube and let NH_3 vapor enter on the right end. Let A be the concentration of $\text{HCl}_{(g)}$, B the concentration of NH_3, C the concentration of $\text{NH}_4\text{Cl}_{(g)}$, and P the concentration of $\text{NH}_4\text{Cl}_{(s)}$. Then using the nucleation and growth model in conjunction with the law of mass action for equations 2.1 and 2.2 yields

$$\frac{\partial A}{\partial t} = D_A \frac{\partial^2 A}{\partial x^2} - K_1 AB \tag{2.3}$$

$$\frac{\partial B}{\partial t} = D_B \frac{\partial^2 B}{\partial x^2} - K_1 AB \tag{2.4}$$

$$\frac{\partial C}{\partial t} = D_C \frac{\partial^2 C}{\partial x^2} + K_1 AB - K_2 f(C, P) \tag{2.5}$$

$$\frac{\partial P}{\partial t} = K_2 f(C, P) \tag{2.6}$$

where D_A, D_B, D_C are the diffusion coefficients of the respective gases and K_1 and K_2 are rate constants. We assume that there is enough HCl and NH_3 gas available that it can diffuse continuously without the concentration changing. Thus the boundary conditions are

$$
\begin{aligned}
A(0, t) &= A_0 & \frac{\partial A}{\partial x}(L, t) &= 0 \\
\frac{\partial B}{\partial x}(0, t) &= 0 & B(L, t) &= B_0 \\
\frac{\partial C}{\partial x}(0, t) &= 0 & \frac{\partial C}{\partial x}(L, t) &= 0 \\
\frac{\partial D}{\partial x}(0, t) &= 0 & \frac{\partial D}{\partial x}(L, t) &= 0
\end{aligned}
$$

where A_0 and B_0 are the initial concentrations of HCl and NH_3 and L is the length of the tube. The initial conditions are

$$A(x,0) = B(x,0) = C(x,0) = P(x,0) = 0 \qquad (2.7)$$

to match the experiments of Singh [23].

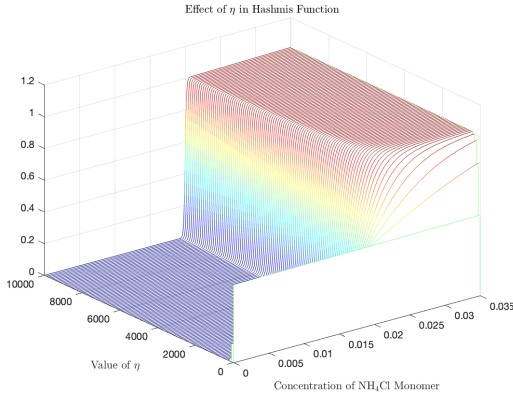The nucleation function $f(C,P)$ used here is called Hashmi's function and is a smoothed version of the piecewise Keller-Rubinow model from Equation 1.11. Let c_{het} be the heterogeneous nucleation threshold and c_{hom} the homogeneous nucleation threshold. Then Hashmi's function [11] is given by

$$f(C,P) = \frac{(C + \gamma - \phi e^{-\nu P})^{\eta+1}}{1 + (C + \gamma - \phi e^{-\nu P})^{\eta}}$$
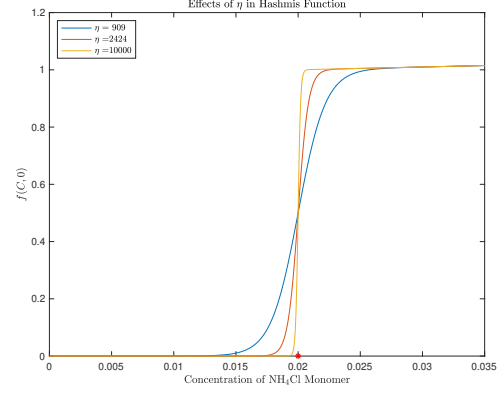
where $\gamma = 1 - c_{het}$ and $\phi = c_{hom} - c_{het}$. The dimensionless parameter η effects the steepness of the function around the nucleation threshold, as shown in Figure 2.1. The larger that η is, the more accurately Hashmi's function mimics the Keller-Rubinow piecewise function. The dimensionless parameter ν only plays a role when there is precipitate present and influences the nucleation threshold as the function transfers between the homogenous and heterogeneous nucleation threshold, as seen in Figure 2.2 . The commonalities between Hashmi's function and the Keller-Rubinow function (Equation 1.11) are seen by considering the extreme cases of precipitate concentration. If $P = 0$ (there is no $NH_4CL_{(s)}$ present), then

$$f(C,0) = \frac{(C + 1 - c_{hom})^{\eta+1}}{1 + (C + 1 - c_{hom})^{\eta}}$$

and f is only a function of the concentration of $NH_4CL_{(g)}$ and begins increasing rapidly at the homogeneous nucleation threshold, as shown by Figure 2.1b. Figure 2.1a shows the behavior of Hashmi's for values of η between 0 and 10000. When η is large, Hashmi's function mirrors the behavior of the step function in the Keller-Rubinow equation very nicely. However, as η approaches

(a) The effects of η for $0 \leq \eta \leq 1000$.

(b) As η increases, Hashmi's function better approximated the Keller-Rubinow piecewise function.

Figure 2.1: The parameter η affects the steepness of Hashmi's function near the nucleation threshold. As η increases, Hashmi's function better approximates the Keller-Rubinow piecewise function. Notice that regardless of η, the inflection point of the function always occurs at the homogeneous nucleation threshold.

0, $f(C, 0)$ approaches the function

$$f = \frac{(C + 1 - c_{hom})}{2}$$

which is far from the desired behavior of the function. The ideal nucleation function should be zero for $C = 0$ and as close to 0 as desired $C < c_{hom}$.

At the other extreme, if P grows, then $\phi e^{-\nu P}$ approaches zero. Mathematically,

$$f(C, P) \underset{P \to \infty}{\to} \frac{(C + 1 - c_{het})^{\eta+1}}{1 + (C + 1 - c_{het})^{\eta}} \tag{2.8}$$

This models the heterogeneous nucleation threshold driving nucleation when some solid is already present. The parameter ν influences how quickly the function transitions between the homogeneous and heterogeneous nucleation threshold as shown in Figure 2.2. When ν is small, a larger amount of precipitate is necessary for Hashmi's function to behave like a piecewise function at the heterogeneous nucleation threshold. However, ν does not have to be very large to make Hashmi's function transition quickly between the two thresholds. Under our assumption, particles only het-
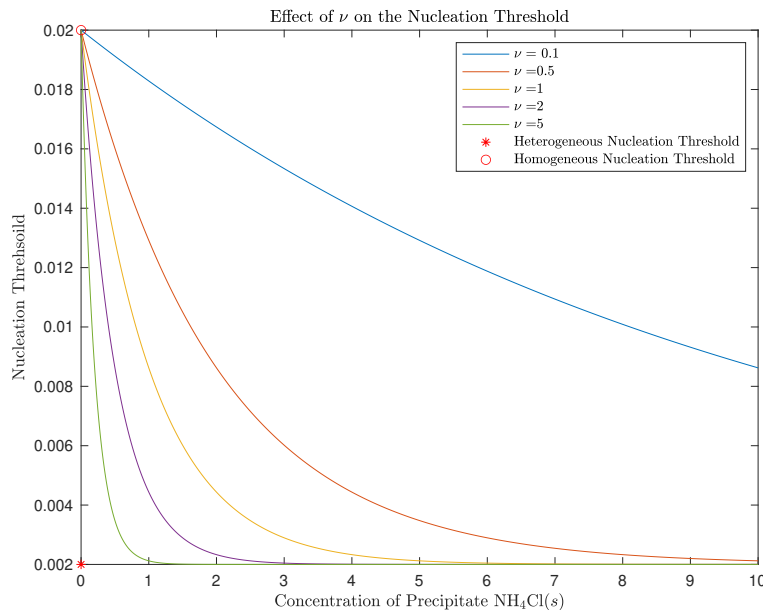
15

Figure 2.2: Effects of ν on the nucleation threshold. Notice that as ν becomes smaller, Hashmi's function transitions between the heterogeneous and homogeneous nucleation threshold quicker.

erogeneously nucleate once any amount of precipitate is present, so we want the transition between thresholds to be very fast.

Hashmi's function produces Liesegang rings and results are shown in Section 2.1.3. However, there are some drawbacks to this function. When $C = 0$, Hashmi's function is close to zero but not quite zero. Thus this function would suggest that participate is formed even when no monomer is present. We also saw that Hashmi's function tends to best estimate our desired step function when η is quite large and ν is rather small. These differences in orders of magnitude can made the function rather stiff and more challenging to numerically simulate.

2.1.2 Front Behavior and Oscillations

There are three major places of interest in the counterdiffusion experiment: the location where $NH_4CL_{(g)}$ first forms (x_i), the location of the first Liesegang ring (x_n), and the ending location of the reaction front (x_f). The initial concentrations of HCl and NH_3 and their diffusivities determine these locations and influence the overall likelihood of Liesegang pattern formation. Let A_0 be the initial concentration of HCl on the left end of a tube and B_0 the initial concentration of NH_3 on the

16

right end on the tube. They have the corresponding diffusion coefficients: D_A and D_B. As given by Thompson et al. [27], the location of first formation of $NH_4CL_{(g)}$ monomer is

$$x_i = \frac{L}{1 + \sqrt{\frac{D_B}{D_A}}} \tag{2.9}$$

where L is the length of the tube. The final front location is

$$x_f = \frac{L}{1 + \frac{D_B}{D_A}\frac{B_0}{A_0}} \tag{2.10}$$

There is no empirical function to predict the location of the first Liesegang ring. However, it is a safe assumption that $x_i < x_n \leq x_f$ since the reaction front travels predominately monotonically in a given direction. This direction is determined by the ratio of the initial concentration of reactants, $\frac{A_0}{B_0}$, in relation to $\sqrt{\frac{D_B}{D_A}}$. The front travels to the right ($x_f > x_i$) if $\frac{A_0}{B_0} > \sqrt{\frac{D_B}{D_A}}$ and the front travels to the left ($x_f < x_i$) if $\frac{A_0}{B_0} < \sqrt{\frac{D_B}{D_A}}$. See Figure 2.3 for a summary of this. The diffusion coefficient for HCl is 0.16 cm^2/s and the diffusion coefficient for NH_3 is 0.22 cm^2/s [27]. Thus if we measure the tube from left to right, the monomer is typically formed approximately $2/5$ of the way down the tube, as reflected in Figure 2.3.

If $\frac{A_0}{B_0} = \sqrt{\frac{D_B}{D_A}}$, then $x_i = x_f$. In this scenario, we would not expect to see Liesegang ring formation and in fact there is likely some tolerance T where if $|x_f - x_i| \leq T$, Liesegang rings would not be able to form. For example, if d is the distance between the first and second Liesegang ring, then if $|x_f - x_i| \leq d$, there is virtually no chance of Liesegang formation. The front must travel sufficiently far to form patterns since front movement is part of what allows for periodic precipitation.

2.1.3 Numerical Results

Numerical results of the nucleation and growth model were generated in MATLAB using the solver pdepe. These results are compared to the data from Singh [23] and Section 2.1.2. Figure 2.4 shows the ring formation of two simulations of the classical nucleation model using Hashmi's
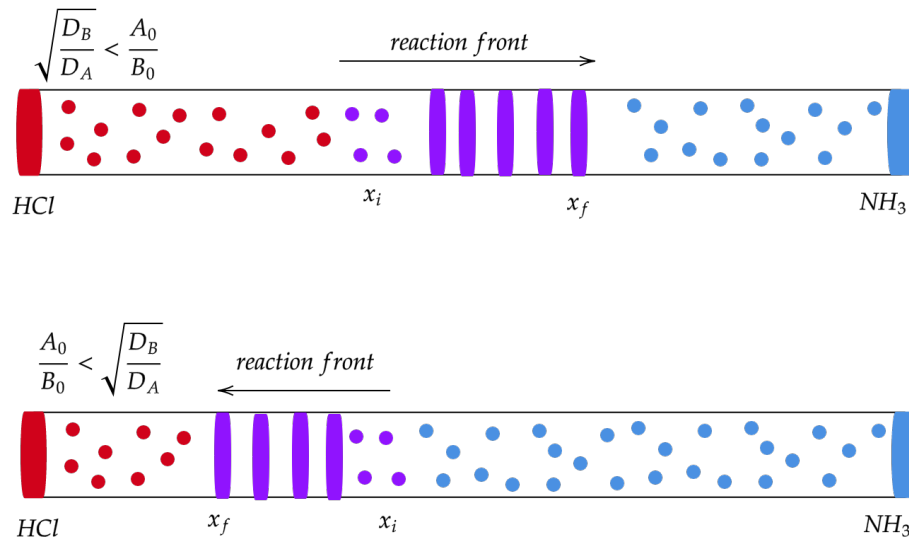
17

Figure 2.3: For the ammonium chloride system, the reaction begins approximately 2/5 of the way down the tube. The direction that the front then travels depends on the ratio of concentration of reactants in relationship to the ratio of their diffusivities.

function. In Figure 2.4a, the ratio of the concentrations of HCl to NH_3 is approximately 0.27 and thus the reaction front travels to the left. In Figure 2.4b, the ratio of HCl to NH_3 is 6 and thus the reaction front travels to the right. In both simulations, precipitate begins forming close to the location of first monomer formation. The final front location, calculated using equation 2.10, is marked by a yellow star. Both fronts travel to approximately this location.

In these results, notice that there is some concentration of $NH_4CL_{(s)}$ between some of the rings. This is possible in some cases [14], so this result can be physical. Singh also notes in his experiments that after the initial ring formation, fainter rings are formed in the void space between the original rings [23]. This observation by Singh could perhaps support some sort of postnucleatioin theory of pattern formation. However, since this model uses only prenucleation theory, the nonzero concentration of precipitate between rings is purely due to the fact that Hashmi's function is always nonzero.

The concentrations used here are not the same as the concentration of reactants used by Singh, so it is not possible to perfectly compare these results to Singh's data [23]. The primary reason why the concentrations that Singh used are not used here is because the solver struggled to solve
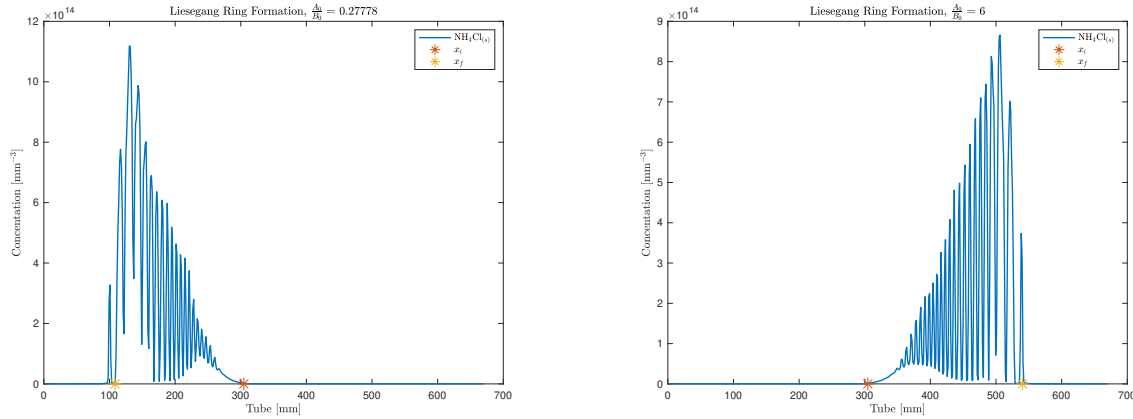
(a) The ending Liesegang pattern using $\frac{HCl}{NH_3} = 0.28$.

(b) The ending Liesegang pattern using $\frac{HCl}{NH_3} = 6$.

Figure 2.4: These plots reflect the two scenarios shown theoretically in Figure 2.3. Based on these results, solid NH_4Cl forms almost immediately after the initial location of monomer formation, x_i. The fronts also end almost exactly where equation 2.10 predicts.

the system given those concentrations. This is likely due to the PDE being stiff, and a future goal is to use a different method to solve the PDE. Singh does however note that in these reactions, the spacing between rings should decrease as times goes on because the reaction front slows down [23]. The results here seem to show no change or a slight increase in ring spacing as time goes on, which is opposite of Singh's observation. One can conclude that this nucleation and growth model does produce Liesegang rings that follow the general front laws outlined in Section 2.1.2. However, the model does not capture the entire behavior of the reaction according to Singh's observations.

The following sections explore new models for this reaction where we focus on the behavior of individually sized gas and solid particles in the system. This way, we may be able to better model the true behavior of the system.

2.2 An Introduction to Coagulation

This section detours into the mechanics and theory of coagulation and the role it plays in the growth of particles - be those gas particles or solid, nucleated particles. This theory is important to understand the models in Sections 2.3 and 2.4. Coagulation (which is used interchangeably with the term agglomeration here) looks at the more microscopic behaviors in particles. For example,

we can consider the behavior of single gas particles, called monomers, or clusters of gas particles, called i-mers, where i correspond to the number of monomers in the cluster. We can also use properties of these i-mers such as their diffusivity and average velocity to determine the likelihood that they collide with another particle and form a larger particle. This process is coagulation.

2.2.1 The Smoluchowski Coagulation Equation

In the simplest scenario, imagine that at time zero we have a box of monodisperse particles – particles of the same species and size. These particles begin moving, following the laws of Brownian diffusion. The particles collide at a rate $K_{i,j}$ which is unique to the two particles i and j that collide. We assume that each collision results in coagulation, although this is not necessarily true in practice. A term can be added to account for this collision efficiency. The growth of particles via coagulation is modeled using an ODE called the Smoluchowski coagulation equation [24].

Each ODE consists of a gain term and a loss term to account for the particles of size i gained from coagulation of smaller particles and the particles lost to growth of larger particles. Refer to Figure 2.5 for a visual of the coagulation of particles. Given infinite time, we assume that particles can grow infinitely large. These assumptions give way to the discrete Smoluchowski coagulation equation, first used by Polish physicist Marian Smoluchowski [24]

$$\frac{dN_i}{dt} = \frac{1}{2}\sum_{j=1}^{i-1} K_{j,i-j} N_j N_{i-j} - N_i \sum_{j=1}^{\infty} K_{j,i} N_j \qquad (2.11)$$

N_i is the number concentration of particles of size i (i.e. a particle consisting of i monomers) or the concentration of particles in bin i if there are too many particles to individually track them by their individual sizes. This first interpretation is used in the kinetic theory growth model in Section 2.3 and the later is used to model the growth of already nucleated particles in Section 2.4. We divide the first term by two since the sum will double count $K_{i,j}$ and $K_{j,i}$.

The Smoluchowski coagulation equation assumes homogeneous mixing. However, for the counterdiffusion experiment, we also care about the location of each particle in relation to the others. Thus we want to extend the Smoluchowski coagulation equation to a partial differential
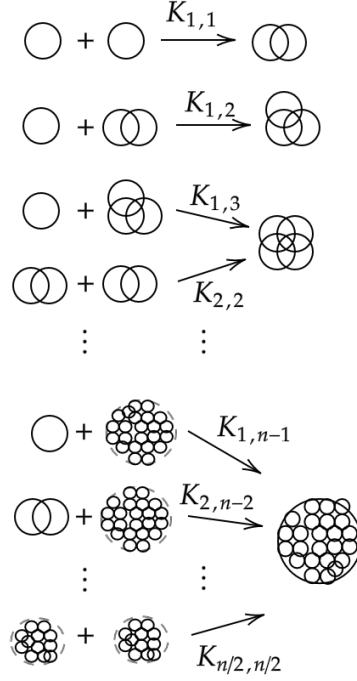
20

Figure 2.5: A visualization of the coagulation of particles. We assume that all collisions result in coagulation and thus the coagulation rate between a particle i and a particle j is represented by the coagulation kernel $K_{i,j}$. In this figure, i and j directly refer to the number of monomers in that particle.

equation. This is done via the Smoluchowski coagulation diffusion equation, which is thoroughly analyzed by Alan Hammond [10]. If we think about how particles behave in a spatial and temporal setting, we should expect that they collide and grow via coagulation but also diffuse throughout they space that they occupy. This concept gives way to the Smoluchowski coagulation diffusion equation:

$$\frac{\partial N_i(x,t)}{\partial t} = D_i \frac{\partial^2 N_i}{\partial x^2} + \frac{1}{2}\sum_{j=1}^{i-1} K_{j,i-j} N_j N_{i-j} - N_i \sum_{j=1}^{\infty} K_{j,i} N_j \tag{2.12}$$

where D_i is the diffusion coefficient for the given particle. Here, $N_i(x,t)$ should be thought of as the number concentration of particles of size i in a small ball around x at time t. The second term is the coagulation growth term which accounts for the growth of a particle of size i from the

coagulation of smaller particles. The last term is the coagulation loss term which accounts for the loss of particles of size i to coagulation with a larger particle.

2.2.2 Coagulation Kernels

The coagulation kernel, $K_{i,j}$ quantifies the likelihood that two particles collide. There are a variety of coagulation kernels used for different particles based on their size and shape. Here, we use some of the most basic coagulation kernels which are outlined by Seinfeld and Pandis [22]. The overarching assumption for these basic coagulation kernels is that the particles are spherical. However particles are often not spherical, so other coagulation kernels exist to account for the different geometries of these particles. Techniques such as fractal dimension are even used to find better suited coagulation kernels as was used by Cho et al. [2].

Size also an important role in the choice of coagulation kernel. Particle behavior can be classified by two molecular regimes, the continuum regime and the free molecular regime (or kinetic regime). Particles are classified into these regimes by their Knudsen number, Kn, a dimensionless parameter equal to the ratio of the particle's mean free path, λ, to its radius r_p [22]

$$Kn = \frac{\lambda}{r_p} \tag{2.13}$$

The Knudsen number is a measurement relating a particle to the space around it. The mean free path of a particle is the average distance traveled by a particle between collisions with other molecules. When Kn is small ($Kn \to 0$), the radius of the particle is larger than its mean free path, so a particle travels less distance than its radius before running into another particle. We use the continuum regime when particles are large. At the opposite end, when Kn is large ($Kn \to \infty$), the radius of a particle is smaller than its mean free path; thus the particle travels farther than its radius before colliding with another particle. This case describes the free molecular or kinetic regime used for small particles [22]. In the continuum regime, traditional fluid mechanics apply. However, for the kinetic regime, the behavior of individual particles becomes important.

Particles do not transition smoothly between regimes. There is a transition regime ($Kn \approx$ 1) where a particle's average distance traveled is approximately equal to its radius [22]. Unless all particles have very small or very large Knudsen numbers, it is common to use functions that smoothly transition between the two molecular regimes.

For particles in the continuum regime, the coagulation kernel is a function of the particles' diameters (D_{p_1} and D_{p_2}) and diffusivities (D_1 and D_2)

$$K_{i,j} = 2\pi(D_{p_1} + D_{p_2})(D_1 + D_2) \tag{2.14}$$

The free molecular coagulation kernel for small particles is a function of the particles' distance form one another and their velocities. Given a particle with radius r_1 and a second particle of radius r_2, the two particles will coagulate if the distance between their centers is less than $r_1 + r_2$. We find the average velocity of a gas molecule as

$$\overline{c_i} = \sqrt{\frac{8kT}{\pi m_i}} \tag{2.15}$$

where k is the Boltzmann constant, T is temperature, and m_i is the mass of the particle. Then the kinetic regime coagulation kernel is

$$K_{i,j} = \pi(r_i + r_j)^2(\overline{c}_i^2 + \overline{c}_j^2)^{\frac{1}{2}} \tag{2.16}$$

The following coagulation kernel accounts for both regimes as well as the transition between them. The correction factor β approaches 1 as the diameter of particles grow, thus bringing the coagulation kernel smoothly from a kinetic to a continuum regime.

$$K_{i,j} = 2\pi(D_i + D_j)(D_{p_i} + D_{p_j})\beta \tag{2.17}$$

Figure 2.6 shows a comparison of the three different coagulation kernels for the interactions between two particles of the same size. Notice that for small diameters, the transition kernel follows

the kinetic regime kernel and for larger diameters, the transition kernel following the continuum regime kernel.
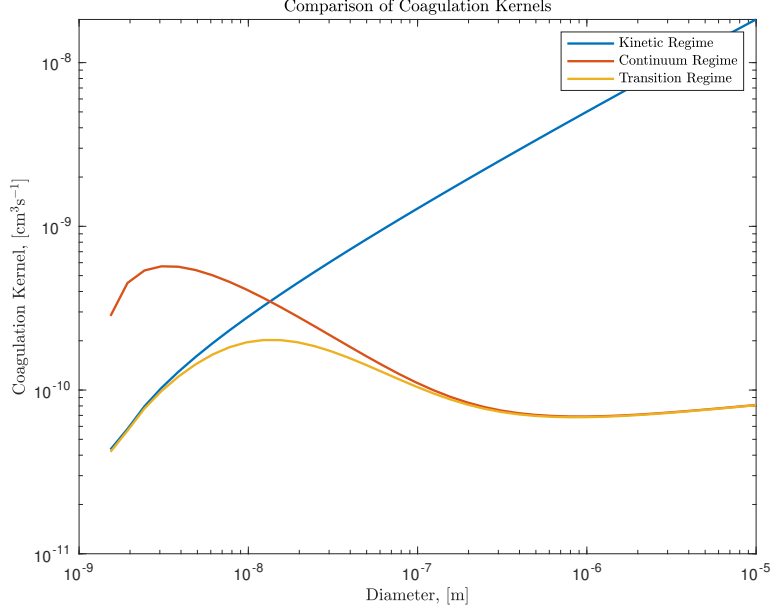

Figure 2.6: A comparison of the molecular regimes for two particles of equal diameter. Here, Fuchs' form of the coagulation kernel is used for the transition regime [22].

2.3 Kinetic Theory of Nucleation

The kinetic theory of nucleation takes a slightly different approach to nucleation, although parallels can be drawn between the core concepts of kinetic and classical nucleation theory. The classical nucleation theory models nucleation at a macroscopic level whereas kinetic nucleation theory looks a nucleation from a microscopic level by tracking individual particles in the system. We begin with a concentration of monomer gas. Over time, these particles move around following the laws of Brownian motion and run into one another. Two monomers form a dimer, a monomer and a dimer form a trimer, and so on. According to Seinfeld and Pandis, collisions between two different size i-mers are rare in gases, and thus we assume that particles grow via collisions only

with monomers [22]. Once the i-mers pass a critical cluster size of n monomers in a cluster, nucleation occurs.

2.3.1 Kinetic Nucleation and Growth Model

For sufficiently large particles, coagulation is permanent. That is, once two particles stick together, they have formed a new, stable particle whose size is equivalent to the sum of the two that collided. However, coagulation is reversible for small particles, and they can dissociate [20]. In fact, up until nucleation, the rate of dissociation is thought to be larger than the rate of coagulation, although their difference decreases as the particle approaches its critical cluster size.

The rate of coagulation, K_i^+, is a coagulation kernel between an i-mer and a monomer. The coagulation rate increases as monomers interact with larger i-mers. At the same time, there is a competing dissociation rate, K_i^-, modeling the rate at which an i-mer breaks down into a monomer and an $(i-1)$-mer. Cluster to cluster interactions are quite rare and the model assumes that i-mers grow and shrink monomer by monomer. Refer to Figure 2.7 for a visualization of this. Using this theory, we can derive a model for the evolution of particles.

Let $N_i(t)$ be the number concentration of clusters containing i monomers at time t. Let K_i^+ be the rate at which a monomer and an i-mer form an $(i+1)$-mer and K_i^- the rate at which an $(1+i)$-mer breaks down into a monomer and an i-mer. Then the change in concentration of an i-mer for $i \geq 2$ is

$$\frac{dN_i}{dt} = K_{i-1}^+ N_1 N_{i-1} + K_i^- N_{i+1} - K_i^+ N_1 N_i - K_{i-1}^- N_i \tag{2.18}$$

with special cases for $i = 1$:

$$\frac{dN_1}{dt} = 2K_1^- N_2 + \sum_{i=3}^{CCS} -2K_{i-1}^- N_i - 2K_1^+ N_1^2 - \sum_{i=2}^{CCS} K_i^+ N_1 N_i \tag{2.19}$$

The first term of Equation 2.18 is the coagulation growth term that accounts for the i-mers gained from the collision of a monomer and an $(i-1)$-mer. The second term is the disassociation
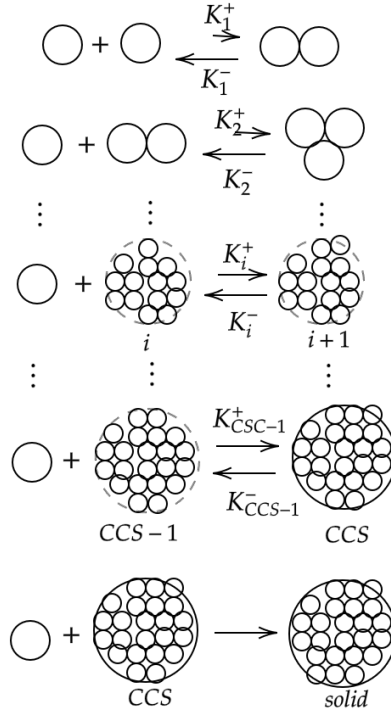
25

Figure 2.7: The growth of i-mers until nucleation after critical cluster size CCS. Notice that as i increases, the values of K_i^+ and K_i^- converge.

growth term, accounting for the growth from an $(i + 1)$-mer dissociating. The third term is the coagulation loss term, which models the i-mers lost by coagulation to a particle of size $i + 1$. Lastly, the fourth term is the dissociation loss term, showing the loss of i-mers to dissociation. The case for $i = 1$ follows a similar interpretation, however there is no coagulation growth term since there is no particle size smaller than a monomer. There is no dissociation loss term for the same reason. Since monomers are so fundamental in the growth of all particle sizes, Equation 2.19 must account for the concentration of monomers decreasing every time a monomer bonds with any i-mer and increasing when a larger i-mer dissociates. CCS stands for critical cluster size.

As previously mentioned, the forward growth rate K_i^+ is derived from the coagulation kernel where we only consider the coagulation of monomers with other particles. Since all particles are a nanometer in size or less, we can use the free molecular coagulation kernel from Equation 2.16. We make some substitutions to write the kernel in terms of i-mers. First, let m denote the mass of

26

a monomer. Then the mass of an i-mer is $m_i = im$. We also assume that all i-mers are spherical, although this assumption does not hold as well for small i-mers. Under this assumption, we write the radius of an i-mer as

$$r_i = \left(\frac{3m_i}{4\rho\pi}\right)^{\frac{1}{3}} \tag{2.20}$$

where ρ is the density of the gas. Then using Equation 2.16, the forward rate is

$$K_i^+ = \sqrt{\pi 8kT}\left(\frac{1}{m} + \frac{1}{m_i}\right)^{\frac{1}{2}}(r + r_i)^2 \tag{2.21}$$

The backward rate constant K_i^- is harder to evaluate theoretically. The only restriction for the backward rate constant is that $K_i^- < K_i^+$ when $i < CCS$ and $K_i^- = K_i^+$ when $i = CCS$ [22]. After nucleation, $K_i^+ > K_i^-$. Section 2.3.2 explores some possible functions for K_i^-.

Notice that Equation 2.18 assumes that particles are spatially homogeneous. However, in a full model for the counterdiffusion of ammonia and hydrochloric acid in a tube, we care about *where* these particles are since their location dictates where nucleation occurs and thus where rings are formed. Thus we expand Equation 2.18 to include a spatial dimension in the same way that the Smoluchowski coagulation diffusion equation does in Equation 2.12.

To develop a full kinetic nucleation and growth model, we make a few more assumptions. We assume that HCl and NH_3 form single $NH_4CL_{(g)}$ monomers. Then these monomers grow via monomer growth. Once the critical cluster size CCS is achieved, the $CCS + i$-mer is considered nucleated material where dissociation no longer occurs. This concentration is denoted N_P. This yields the following model

$$\frac{\partial A}{\partial t} = D_A\frac{\partial^2 A}{\partial x^2} - K_1 AB \tag{2.22a}$$

$$\frac{\partial B}{\partial t} = D_B\frac{\partial^2 B}{\partial x^2} - K_1 AB \tag{2.22b}$$

$$\frac{\partial N_1}{\partial t} = D_1\frac{\partial^2 N_1}{\partial x^2} + K_1 AB + 2K_1^- N_2 + \sum_{i=3}^{CCS} -2K_{i-1}^- N_i - 2K_1^+ N_1^2 - \sum_{i=2}^{CCS} K_i^+ N_1 N_i \tag{2.22c}$$

$$\vdots \tag{2.22d}$$

$$\frac{\partial N_i}{\partial t} = D_i \frac{\partial^2 N_i}{\partial x^2} + K_{i-1}^+ N_1 N_{i-1} + K_i^- N_{i+1} - K_i^+ N_1 N_i - K_{i-1}^- N_i \tag{2.22e}$$

$$\vdots \tag{2.22f}$$

$$\frac{\partial N_{CCS}}{\partial t} = D_{CCS} \frac{\partial^2 N_{CCS}}{\partial x^2} + K_{i-1}^+ N_1 N_{i-1} - K_{CCS}^+ N_1 N_{CCS} - K_{CCS-1}^- N_{CCS} \tag{2.22g}$$

$$\frac{\partial N_P}{\partial t} = D_P \frac{\partial^2 N_P}{\partial x^2} + K_{CCS}^+ N_1 N_{CCS} \tag{2.22h}$$

We assume that there is no NH_3 or HCl present in the tube initially, so the initial conditions are

$$A(x,0) = B(x,0) = N_i(x,0) = 0 \tag{2.23}$$

The boundary conditions are also similar to those of the classical model. We allow hydrogen chloride to diffuse in from the left and ammonia from the right and have zero flux otherwise.

$$A(0,t) = A_0 \quad \frac{\partial A}{\partial x}(L,t) = 0 \tag{2.24a}$$

$$\frac{\partial B}{\partial x}(0,t) = 0 \quad B(L,t) = B_0 \tag{2.24b}$$

$$\frac{\partial N_1}{\partial x}(0,t) = 0 \quad \frac{\partial N_1}{\partial x}(L,t) = 0 \tag{2.24c}$$

$$\vdots \tag{2.24d}$$

$$\frac{\partial N_P}{\partial x}(0,t) = 0 \quad \frac{\partial N_P}{\partial x}(L,t) = 0 \tag{2.24e}$$

This kinetic approach still follows the nucleation and growth models outlined in Section 1.2.1. However in this model, the step $C \rightarrow P$ is now broken into many small steps. The hope is that this approach captures more of the true behavior of the system and produce more accurate results than those from Hashmi's function.

2.3.2 Numerical Results of a Spatially Homogeneous Kinetic Model

In this section, we numerically simulate the a spatially homogeneous kinetic growth model and consider possible dissociation rates. The spatially homogeneous model simply removes the spatial

component from Equation 2.22. Given the constraints previously outlined for the dissociation rate, three different equations for the dissociation rate are proposed. All of them are functions of the growth rate and i-mer size. The first dissociation rate has the most variance from the growth rate for all i.

$$K_1^- = K_i^+ \left(\frac{CCS - 1}{i} \right) \tag{2.25}$$

The second dissociation rate linearly decreases to approach K_{CCS-1}^+:

$$K_i^- = -K_i^+ + 2K_{CCS-1}^+ \tag{2.26}$$

The third function is non-linear, but quickly reaches the values of K_{CCS-1}^+. This function has the least variance from the growth rate for all i.

$$K_i^- = \frac{K_{CCS-1}^+}{2i^{i-1}} + K_{CCS-1}^+ \tag{2.27}$$

Refer to Figure 2.8a for a plot of the different functions for $i \in \{1, 2 \ldots, 23\}$. In this case, the critical cluster size is 23 and thus $K_{22}^+ = K_{22}^-$.

Each dissociation function has an effect on on the growth of particles. Figure 2.8b shows the results of using different dissociation rates. Using the first dissociation rate leads to the fastest nucleation, which is a rather counter-intuitive result. One might at first believe that a large dissociation rate should make nucleation harder to achieve and therefore take longer; after all, a large dissociation rate means that i-mers are *more* likely to fall apart than stick together. The following sub subsection is dedicated to justifying this result.

The power of monomers

If we allowed this system to run for an infinite amount of time, the system would reach what we call a steady state where concentrations are no longer changing over time. Mathematically, this is equivalent to $\frac{dN_i}{dt} = 0$ for all $i \in \{1, \ldots, CCS + 1 = P\}$. Notice that in the previous model from Equation 2.22 the steady state solution of the system is $N_i = 0$ for $i \in \{1, \ldots, CCS\}$ and
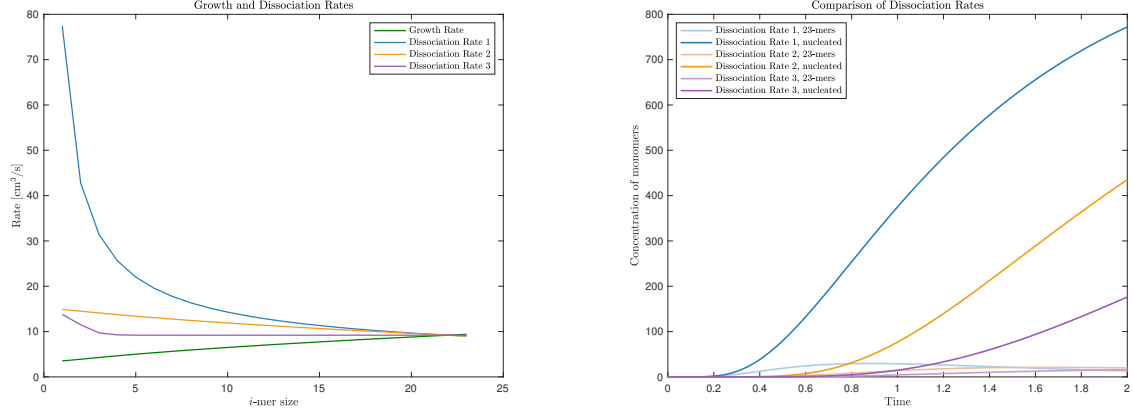
(a) The growth rate and three dissociation rates given by Equations 2.25, 2.26, 2.27.

(b) The evolution of particles of critical cluster size (23-mers) and growth of the corresponding nucleated particles (24-mers), compared for the three different dissociation rates. Notice the clusters are plotted in terms of the number of monomers. So, a concentration of 600 monomers for nucleated 24-mers would convert to a number concentration of 25 24-mers per unit volume.

Figure 2.8: The dissociation rates and their corresponding nucleation results. The system was set up with an initial monomer concentration of 1000 m^3.

$N_P = N_1(0)$. To better understand the results shown in Figure 2.8, we will use a model which produces the same qualitative results but does not have the same steady state solution, since it is likely not completely physical anyway. Once introducing the modified model, we will explore an intuitive explanation as to why the results shown in Figure 2.8 make sense given the following model. We can then justify some claims made in this intuition mathematically.

The one change in this model is that the dissociation rate $K_{CCS}^- \neq 0$. Thus Equation 2.22h now has a dissociation loss term instead of only a coagulation growth term.

$$\frac{\partial N_P}{\partial t} = D_P \frac{\partial^2 N_P}{\partial x^2} + K_{CCS}^+ N_1 N_{CCS} - K_{CCS}^- N_P \tag{2.28}$$

and Equation 2.22g now picks up a dissociation growth term

$$\frac{\partial N_{CCS}}{\partial t} = D_{CCS} \frac{\partial^2 N_{CCS}}{\partial x^2} + K_{i-1}^+ N_1 N_{i-1} - K_{CCS}^+ N_1 N_{CCS} - K_{CCS-1}^- N_{CCS} + K_{CCS}^- N_P \tag{2.29}$$
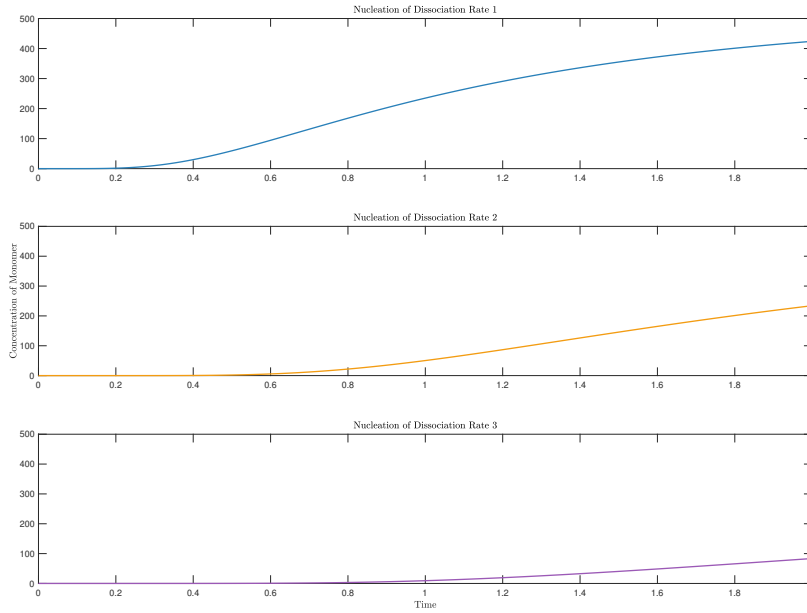
Figure 2.9: A comparison of the growth of precipitate (24-mers) for the three dissociation rates. Notice that using dissociation rate 1 results in nucleation happening first. Results come from the modified model with modification shown by equations 2.28 and equation 2.29.

We also again simplify this model to be spatially homogeneous, simplifying the model to an ODE. The results of this model, shown in Figure 2.9, are qualitatively the same as the results in Figure 2.8b. The only difference is the steady state concentrations. This allows us to gain some more intuition about the system as a whole.

Recall that we assume particles grow monomer by monomer, as outlined by the model in Equation 2.18. Thus it is absolutely imperative that monomers are present in order for an i-mer to grow, and in fact a larger concentration of monomers leads to faster growth. Now suppose we compare two dissociation rates – we'll call them dissociation A and dissociation B. Dissociation A is much larger than dissociation B for all i-mer sizes (much as if we are comparing dissociation rate 1 and dissociation rate 3 from Figure 2.8a.). Since dissociation A is so large, it is more likely that an i-mer breaks apart than it grows. Every time an i-mer dissociates, it loses a monomer. This monomer is now free to move around and coagulate with a fellow monomer or another i-mer. Dissociation A consistently has more monomers than dissociation B. There are enough monomers

31

present that they can act as a catalyst and speed along the growth of i-mers so that dissociation A has particles that nucleate first. Once particles have reached the critical cluster size, the growth rate becomes larger than the dissociation rate, and it is easy for the excess monomers of dissociation A to bond with the critical cluster size and produce large amounts of nucleated material. Since the larger dissociation rate forces there to constantly be more monomers in the system, the overall time for particles to reach a critical cluster size is actually *faster* and dissociation A has a larger concentration of nucleated material than dissociation B.

There are two statements here that are relatively easily to justify mathematically. The first is: there are more monomers present in the system when the dissociation rate is larger. The second is: there is more precipitate present when the dissociation rate is larger. We justify these by solving for the steady state solution: $\frac{dN_i}{dt} = 0$. For systems such as this, we can start with $\frac{dN_P}{dt}$ and work backward. The general process is outlined below.

$$\frac{dN_P}{dt} = 0 = K^+_{CCS} N_1 N_{CCS} - K^-_{CCS} N_P$$
$$\implies N_P = \frac{K^+_{CCS} N_1 N_{CCS}}{K^-_{CCS}}$$
$$\frac{dN_{CCS}}{dt} = 0 = K^+_{i-1} N_1 N_{i-1} - K^+_{CCS} N_1 N_{CCS} - K^-_{CCS-1} N_{CCS} + K^-_{CCS} N_P$$
$$= K^+_{i-1} N_1 N_{i-1} - K^+_{CCS} N_1 N_{CCS} - K^-_{CCS-1} N_{CCS} + K^-_{CCS} \left(\frac{K^+_{CCS} N_1 N_{CCS}}{K^-_{CCS}} \right)$$
$$\implies N_{CCS} = \frac{K^+_{CCS-1} N_1 N_{CCS-1}}{K^-_{CCS-1}}$$
$$\vdots$$
$$N_i = \frac{K^+_{i-1} N_1 N_{i-1}}{K^-_{i-1}} \text{ for } i = \{2, \ldots, P\}$$

Since this system is conservative, the total number of monomers should remain constant, although some of them now exits as a pair in dimers, a triple in trimers, and so on. Thus we write the total concentration of monomers at steady state as

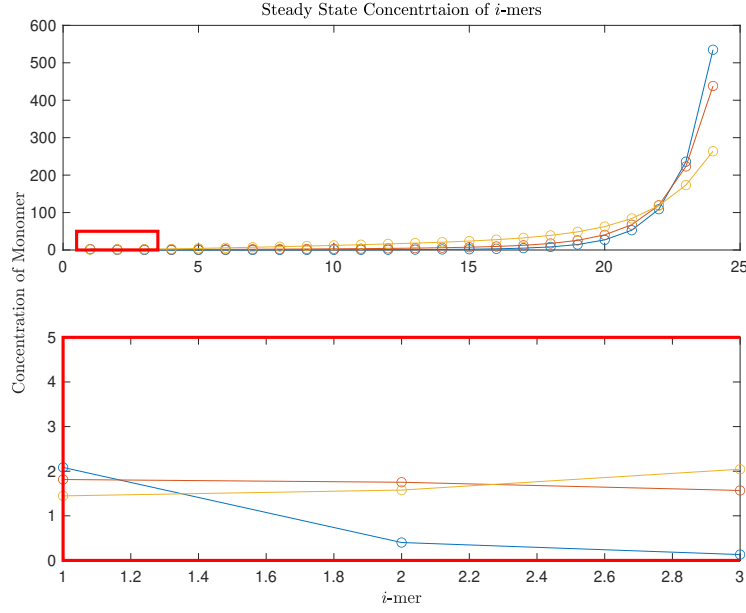$$T = N_1 + 2N_2 + \cdots + CCSN_{CCS} + PN_P \tag{2.31}$$

Figure 2.10: The steady state concentration of i-mers, written in terms of concentration of monomers. Notice that the largest dissociation rate, Dissociation Rate 1, has the most monomers and the most precipitate. The lower plot shows the zoomed in results for monomer, dimers, and trimers. Notice all concentration are given in monomers in order to see how monomers are distributed throughout the differnet sizes.

where T is the initial concentration of monomer $N_1(0)$. With enough substitution, this becomes a polynomial in terms of monomer N_1 since each N_i is

$$N_i = N_1^i \prod_{j=1}^{i} \frac{K_j^+}{K_j^-} \tag{2.32}$$

Solving for N_1 in Equation 2.31 yields the steady state concentration of monomer. Equation 2.32 is then used to find the corresponding steady state concentrations of all i-mers. Figure 2.10 shows the steady state solution of each i-mer for the three dissociation rates. Notice that dissociation rate 1 (the largest) has the most monomer steady state concentration and the most precipitate steady state concentration, even though the steady state concentration of other i-mers is less than the other dissociation rates. This lines up with the intuition we built previously.

While the results of this model make sense *given the model*, it begs the question if this intuition or these results make sense *physically*. There are some possible modifications for this kinetic

theory. Ruckenstein and Berim propose that nucleation is actually driven by two mechanisms [20]. The first mechanism is kinetic growth via monomers as is outlined here. The second mechanism argues that there are some scenarios where the growth rate of a dimer is larger than the dissociation rate of a dimer, and thus this dimer is already as stable as a particle larger than critical cluster size and as such, can "act as the nuclei for aerosol growth" [20]. A possible different modification to the model is to allow particles to grow via more than simply monomer growth. It is assumed that i-mers grow via monomer collisions because cluster-cluster collisions are rare due to the slowness of larger i-mers. However, it is still likely that a dimer collides with a larger i-mer. Thus it may be reasonable to develop a model where growth happens via small i-mer collisions. Although these possible modifications to the model are not explored here, the results from the comparison of the dissociation rates suggest that the monomer growth model on its own may not be a physical model for nucleation and a more sophisticated model may provide more physical results.

2.3.3 The Kinetic Theory of Nucleation and Liesegang Rings

After seeing the theoretical model of monomer growth as the mechanism that leads to nucleation, a natural question to ask is, "Could this even possibly form Liesegang rings?" At first glace, one might think that it would be impossible. After all, this monomer growth model applies to other chemical reactions beyond the $HCl + NH_3$ system, and not all chemical reactions form Liesegang patterns. However, there could possibly be something unique to the true parameters for the $HCl + NH_3$ that would cause Liesegang band formation whereas the true parameters for other reactions would not allow for periodic precipitation. Intuitively, there is a possibility that the kinetic monomer growth model could result in pattern formation.

Refer back to Equation 2.18 and recall the prenucleation theory of Liesegang pattern formation where periodic precipitation occurs because of oscillations in the concentration of $NH_4CL_{(g)}$ during nucleation. Monomers are unique because one of the coagulation loss terms depends on the *square* of monomer $(-2K_1^+ N_1^2)$, so the concentration of monomer should decrease quadratically when there are predominately monomers present. Thus dimers grow quadratically in their coagu-

lation growth term. Because of this non-linearity, we could expect that under the right conditions, monomers become depleted and dimers grow until a tipping point when the dissociation loss term for dimers takes over since $K_1^- >> K_1^+$, depleting dimer concentration and growing monomer concentration again. This could cause oscillations in monomer growth which would then reflect throughout the rest of the i-mers.

This scenario described above is in fact possible under under some artificial parameters. For these next results, we do not consider units for the entire section. In fact, we will slightly change the full kinetic model as described at the end of Section 2.3.1. Suppose that instead of allowing HCl and NH_3 gas to diffuse into the system, creating a front with non constant velocity and concentrations, we instead supply $NH_4Cl_{(g)}$ to the system using a 2D Gaussian-like source term G which is a function of time, t, and location in the tube, x.

$$G(x,t) = 5 \times 10^{-6} \exp(-16(x - 2 - 2t)^2) \tag{2.33}$$

The source term is illustrated in Figure 2.11. Here, monomer gas is supplied at a constant concentration and moves at a constant velocity to the right across the entire tube. This source term is synonymous with a reaction front - although here is it an artificially created reaction front. Also notice the amount of monomer gas is quite small, on the order of 10^{-6}. Higher amounts did not result in oscillations.

Along with the constant supply of monomer gas, we also simplify the forward and backward rates. The growth rate K_i^+ for $i < CCS$ is 0.1 and the growth rate for $i \geq CCS$ is 10. The dissociation rate, K_i^- for $i < CCS$ is 1 and the dissociation rate for $i \geq CCS$ is quite small; only 0.001. We also assume that all clusters diffuse at the same rate of 0.02. Nucleated clusters diffuse more slowly at 0.001. Using the above parameters, the monomer source described by Equation 2.33, and a mesh of $(0, 40)$ for x and $(0, 30)$, for t, we achieve rings! Figure 2.12 show monomer concentration, concentration of 11-mers - about half way through the growth process, concentration of 23-mers (the critical cluster size), and concentration of nucleated particles (24-mers pr nuclei). Notice that the concentrations become incredibly small. Scaling the given Gaussian source term
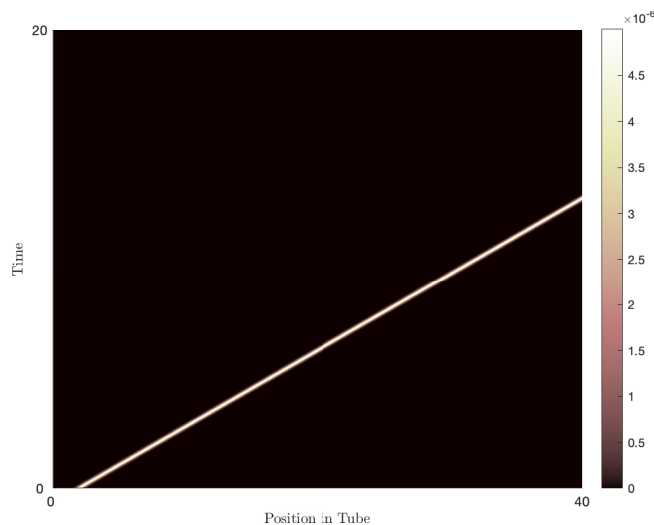
35

Figure 2.11: This plot shows the reaction front as it traveled down the rube. Here, a constant supply of monomer concentration is traveling at a constant velocity to the right across the tube. Notice that the amount of monomer gas - shown by the color-bar - is quite small.

larger stopped oscillations from occurring, so no other parameters were tested for the time being. These results do show that it may be possible to generate Liesegang rings using the kinetic model if given the correct parameters. Although not done here, a future goal is finding more physical parameters for the system and seeing if these parameters result in Liesegang rings as well.

2.4 Modeling the Growth of Nucleated Particles

Thus far, we have only focused on the nucleation process of ammonium chloride. However, once nucleation occurs, these small solid particles grow to thousands of times their original size. Assuming nucleation occurs immediately after a critical cluster size of 23 monomers, each newly nucleated $NH_4Cl_{(s)}$ particle is less than one nanometer in diameter. By the time the experiment is complete and all Liesegang bands have formed, $NH_4Cl_{(s)}$ particles are as large as 5 microns in diameter [23]. This section focuses on modeling the growth of these particles. In this section the word "particle" will refer to a nucleated particle, whereas in previous sections, "particle" was used interchangeably with a gas-phase i-mer.
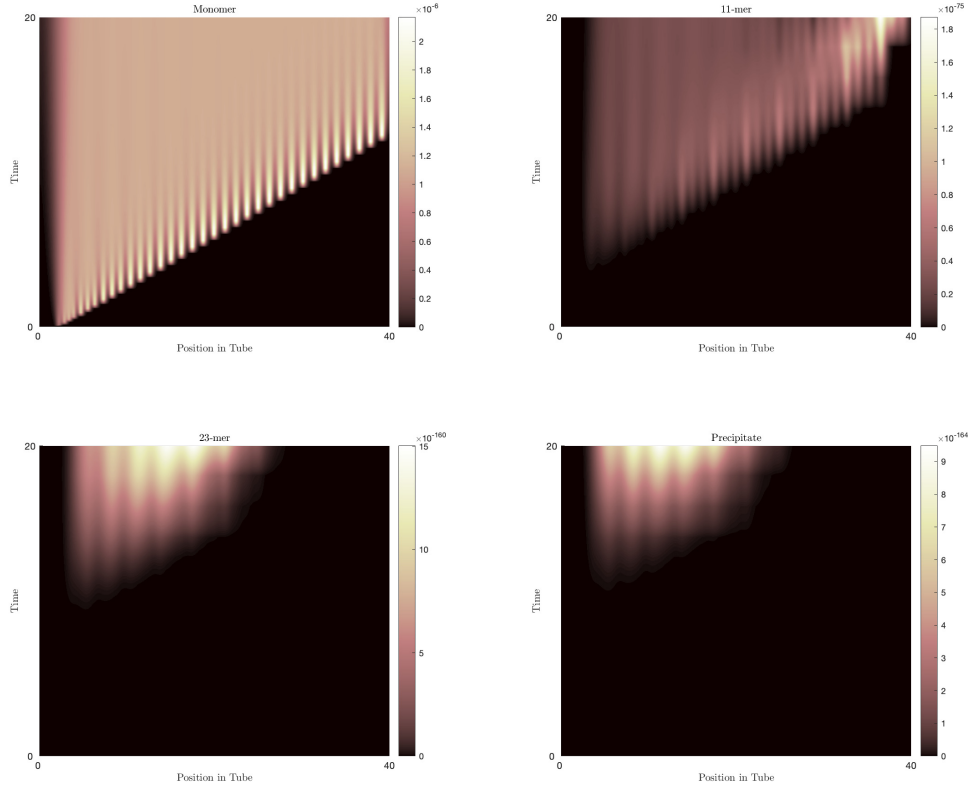
36

Figure 2.12: Plots showing the concentration of i-mers throughout the reaction. We do see oscillations occur, but notice the concentrations are larger i-mers are alarmingly small, suggesting more work must be done to fine tune these parameters.

2.4.1 The Binned Smoluchowski Coagulation Diffusion Equation

A $NH_4Cl_{(s)}$ particle 5 μm in diameter has approximately 1.7×10^{12} monomers, and thus it is not computationally feasible to track the growth of each i-mer. Instead, we can group similarly sized particles into bins and track the growth of the bins instead. A typical binning procedure divides particles into bins using mass doubling. That is, the upper bound of the mass of each bin is twice the mass of the lower bound for that bin - or the mass of the geometric mean of each bin is exactly double the mass of the prior bin. Within each bin, it is assumed that all particles have the same diameter. The diameter of each bin is the geometric mean of that bin.

Nucleated particles grow in a similar manner to their growth pre-nucleation with only a few key differences. First, it is assumed that the particles are now large enough that coagulation is an

irreversible process. Second, we assume cluster to cluster collisions are possible. Using these basic assumptions, we can modify the Smoluchowski coagulation diffusion equation to develop a model for the growth of $NH_4Cl_{(s)}$ bins. We again use a coagulation kernel to account for the likelihood that two particles of given diameters collide and stick together. However, since particles span such a massive size range (less than one nanometer to approximately 5 micrometers), it is necessary to use the transition regime coagulation kernel from Equation 2.17.

The coagulation kernel $K_{i,j}$ corresponds to the interactions between a particle in bin i and a particle in bin j. Because we use a binning method as opposed to i-mer growth, the growth of each bin is different than the growth of i-mers. A particle from bin i colliding with a particle form bin j does not place this particle into bin $i + j$. Two particles coagulating from bin i will certainly allow them to move into bin $i + 1$. However, there is more gray area when we consider a particle from bin i colliding with a particle in bin j where $j > i$. Under the mass doubling, we know this particle should probably remain in bin j, but we also made the assumption that all particles in a bin should have the same diameter when in practice this is not true. Thus we want to allow some particles to grow into bin $j + 1$ to remediate this assumption. We do this using a mass centering method which is outlined below. The following process is also visualized in Figure 2.13 as well.

1. The concentrations of bin i and bin j decrease when a particle from each bin collides.

2. Suppose $j > i$. We distribute most of the grown particles back into bin j. However, we also distribute some into bin $j + 1$ to account for the fact that physically, larger particles exist and could grow into the next bin size. The exact amounts are determined by the the particles masses, as outlined in the Equation 2.34.

3. If $i = j$, then the particle moves into bin $j + 1$.

Using the previous outline, we derive the binned Smoluchowski coagulation diffusion equation:

$$\frac{\partial B_k}{\partial t} = D_k \frac{\partial^2 B_k}{\partial x^2} - \sum_{i=1}^{\text{end - 1}} c(i) K_{k,i} B_k B_i + \sum_{i=1}^{k} K_{k,i} B_k B_i \left(1 - \frac{m_{k,i} - m_k}{m_{k+1} - m_k} \right)$$
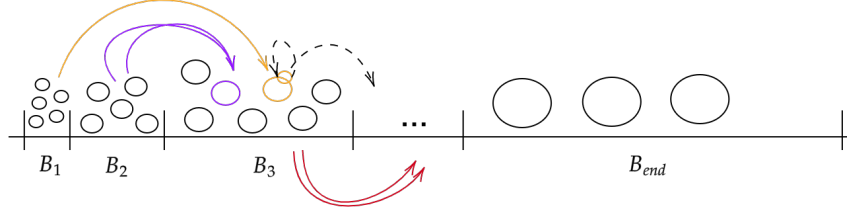
Figure 2.13: A visualization of the binning process. Assuming bins are created based on when the mass of the particle doubles, the change in concentration of a bin is modeled differently than the change in concentration of i-mers. If two particles in bin i coagulate, they move into bin $i + 1$. However, a particle from bin i and bin $j < 1$ could stay in bin i or move into bin $i + 1$, as outlined by Equation 2.34. This approach allows the concentration of particles in a bin to change while preserving bin centers.

$$+ \sum_{i=1}^{k-1} K_{k-1,i} B_{k-1} B_i \left(\frac{m_{k-1,i} - m_{k-1}}{m_k - m_{k-1}} \right) \quad (2.34)$$

where $m_{i,j} = m_i + m_j$ and $c(i) = 2$ if $i = k$ and $c(i) = 1$ otherwise. The first term on the right hand side accounts for the diffusion of particles throughout space. The next term corresponds to number 1 from the previous list. The following two term corresponds to number 2, where the first of the two distributes particles back into bin k and the second term accounts for the particles gained from the redistribution of bin $k - 1$ into bin k. This final term also account for number 3 when $i = k$.

2.4.2 Growth of Liesegang Bands

To test the validly of the binning model from Equation 2.34, we will first simplify the model to the growth of a single Liesegang band. Next, we apply the full model as outlined by Equation 2.34 by building off of the rings produced by Hashmi's function in Section 2.1.

Growth of a Single Band

A single ring is thin enough that we can assume a spatially homogeneous model and thus can eliminate the spatial aspect of the binned Smoluchowski coagulation diffusion equation to instead

have the ODE

$$\frac{dB_k}{dt} = -\sum_{i=1}^{\text{end - 1}} c(i) K_{k,i} B_k B_i + \sum_{i=1}^{k} K_{k,i} B_k B_i \left(1 - \frac{m_{k,i} - m_k}{m_{k+1} - m_k}\right)$$
$$+ \sum_{i=1}^{k-1} K_{k-1,i} B_{k-1} B_i \left(\frac{m_{k-1,i} - m_{k-1}}{m_k - m_{k-1}}\right) \qquad (2.35)$$

where the coagulation kernel itself accounts for the diffusivity of the particles. We assume all particles nucleate at the exact same size and thus provide an initial condition of particles all in the smallest size bin. Given enough time, all particle would move to the largest bin since there is no term to damp the growth of particles. However, we only allow the model to run for an hour, keeping consistent with the true timeline of the counterdiffusion reaction according to Singh's data [23]. Figure 2.14 shows the growth of particles over this hour. Notice that the growth and decay of each concentration after the first bin follows a Gaussian curve. Also note that the units here are measured in nuclei concentration, where "nuclei" refers to a CCS+1-mer; or a freshly nucleated particle. For reference, a single particle in the last bin has 3.4×10^{10} nuclei, so the concentrations here are really quite small. The smaller initial concentration was chosen somewhat arbitrarily, and the hope is to use more physical values in the future. Even with a non-physical initial concentration of nuclei, the qualitative behavior of the system can still be examined.

Singh collected data on the particle size distribution for diameters ranging from approximately 0.5 μm to 3.5 μm and over [23] for 7 rings formed in the tube under a variety of initial concentrations. Figure 2.15a shows Singh's data on the first two rings for an initial concentration of $NH_3 = 18\%(v/v)$, $HCl = 12.1\%(v/v)$, moisture $= 100$ p.p.m. Figure 2.15 then shows the comparison of the particle distribution from the binned Smoluchowski coagulation equation and data from Singh. Recall that in the binned model, bins are created using mass doubling and therefore do not line up perfectly with the bin ranges in Figure 2.15a. To compare the model with Singh's data, each bin from the model was re-binned according to Singh's binning. Under this re-binning process, all bin concentrations that landed within Singh's range were summed and placed into that new Singh bin. For example, the concentration of particles in a size bin whose diameter is 0.55
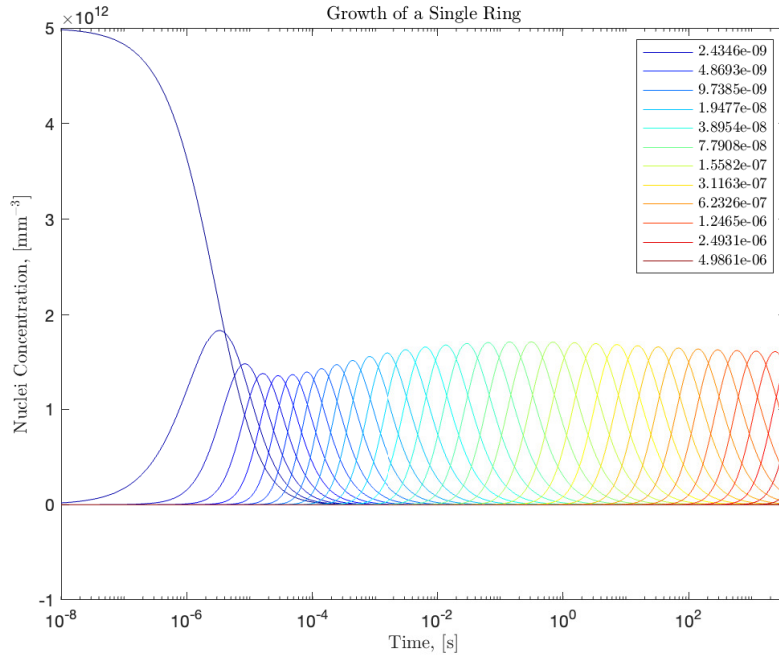
Figure 2.14: The growth of particles in a singe Liesegang band over an hour. Each curve represents the evolution of the concentration of that bin. The legend gives a general idea of the diameter of that size bin, but does not list all bins since there are 36 of them. Note that this concentration counts the number concentration of nuclei (a freshly nucleated, small CCS+1-mer) and not number concentration.

μm were binned into the $0.5 - 1.0$ μm Singh bin. To achieve the plot in Figure 2.15b, an initial concentration of 8×10^{12} particles per mm^3 was used. This concentration created the most similar distributions to Singh's one hour in. Future work remains to determine more physical initial concentrations. Qualitatively, the results form the model are similar to Singh's second ring under these concentrations.

In the future, it would be beneficial to run a model such that the bins perfectly match those of Singh or to find a better method to redistribute the bins into Singh's framework. Singh has data on a number of different reactions all with different concentrations [23]. The change in concentration effects the overall distribution, so not all particle distributions of Singh's look like the one in Figure 2.15a. More work remains to better reproduce all the rings that Singh has distributions for.

(a) Particle size distributions from Singh [23]. No units were provided on his plots.
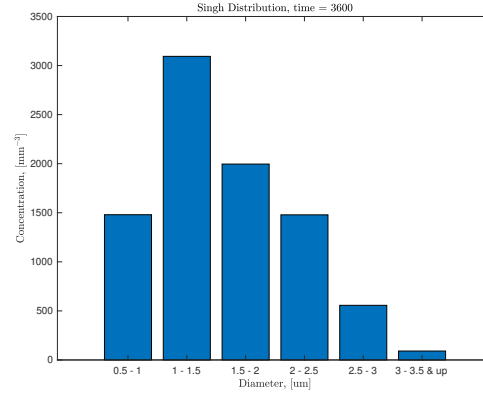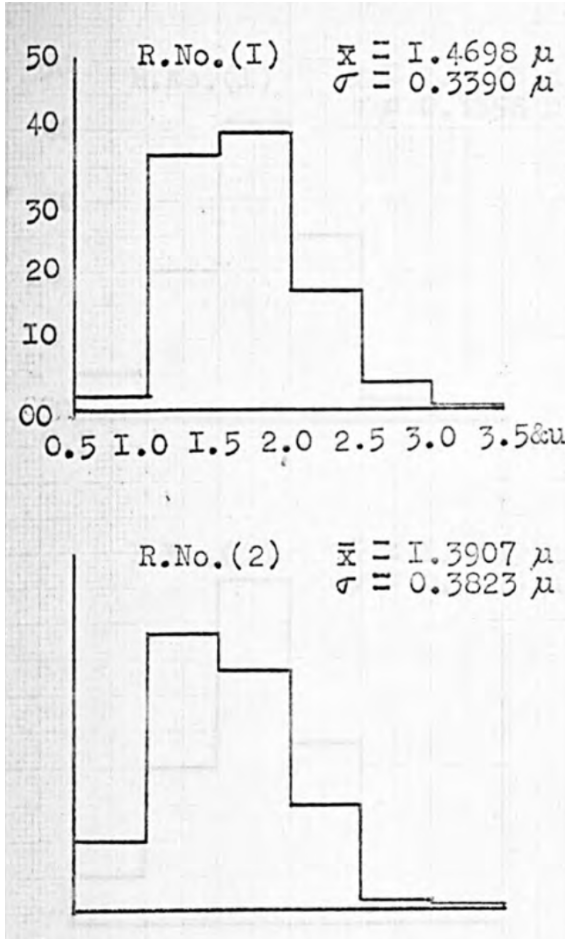
(b) The particle size distribution using the the binned Smoluchowski coagulation equation from equation 2.35, using an initial nuclei concentration of 8×10^{12}.

Figure 2.15: A comparison of Singh's data to the results of the binned Smoluchowski coagulation equation where the initial condition of $NH_4Cl_{(g)}$ is 8×10^{12} particles per mm^3. Singh used a concentration of 18%(v/v) NH_3 and 12.1%(v/v) HCl. Qualitatively, the results are similar to the distribution of the second ring.

Growth of Liesegang Bands

Now that we see promising results from the ODE model of particle growth, we return to the binned Smoluchowski coagulation diffusion equation from Equation 2.34 and combine it with the basic nucleation and growth model from Section 2.1. However, now instead of
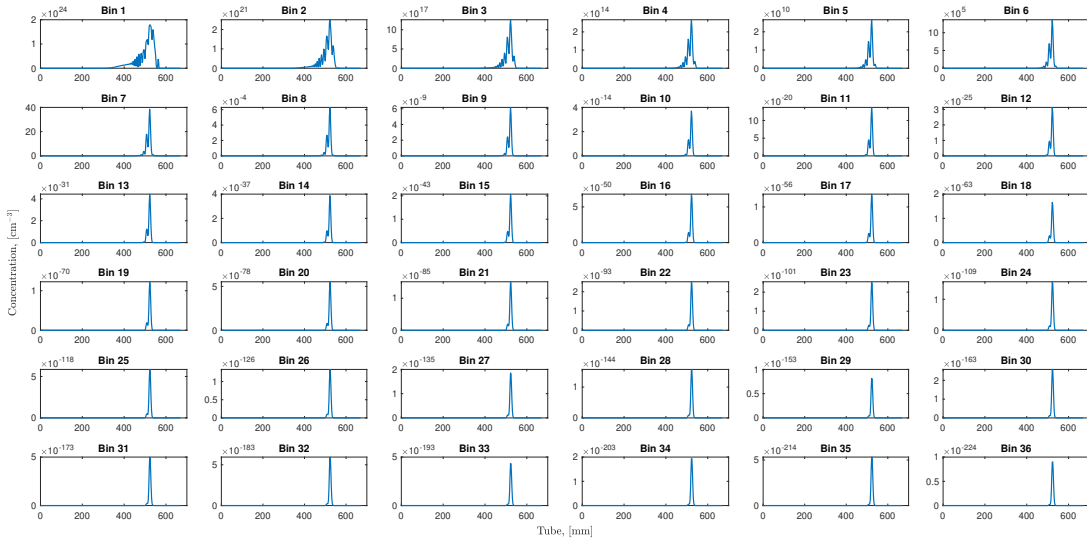
$$HCl + NH_3 \longrightarrow NH_4Cl_{(g)} \longrightarrow NH_4Cl_{(s)} \tag{2.36}$$

42

Figure 2.16: The plot of concentrations of particles and their location for each bin. Notice the concentrations for the larger bins become very small. The smallest bin has particles of diameter 1.5 nm and the largest bin has particles of diameter 5 μm. The initial concentration ratio is $\frac{\text{HCl}}{\text{NH}_3} = 6$ and the other parameters were as the same as those used for Figure 2.4b.

as we had previously, we assume that all monomer nucleates into the first bin, giving

$$\text{HCl} + \text{NH}_3 \longrightarrow \text{NH}_4\text{Cl}_{(g)} \longrightarrow B_1 \tag{2.37}$$
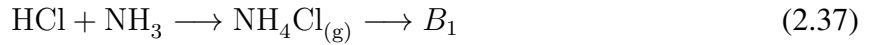
which then grows using the binning model. We use Hashmi's function in terms of $\text{NH}_4\text{Cl}_{(g)}$ and precipitate in the first bin ($f(C, B_1)$) for the mechanism by which $\text{NH}_4\text{Cl}_{(g)}$ nucleates. We can then observe the growth of each Liesegang band, and the results of final particle distributions for each bin are provided in Figure 2.16.

Notice that the orders of magnitudes of the later bins are quite small. This is likely because some of the parameters are non-physical. This choice was partially made because the more physical parameters were too stiff for the solver pdepe. Additionally, using Hashmi's function limits the nucleation mechanism, since using $f(C, B_1)$ assumes that only the particles in the first bin aid nucleation whereas any size of precipitate should air nucleation. This could also contribute to the very small concentrations of larger particles. In the future, a different solver should be used and

43

we would likely see more accurate concentrations. Changing the model to also allow nucleation on larger particles may also be necessary.

The model previously outlined is also the start of a sol-coagulation model in which the growth of nucleated particles is modeled separately from its nucleation step. The following section uses the previous two sections to develop a complete sol-coagulation model.

2.5 A Complete Sol-Coagulation Model

A natural continuation of Liesegang pattern formation modeling is the sol-coagulation model which was described by Equations 1.13, 1.14, 1.15. This section briefly outlines a sol-coagulation model which builds on the models from Sections 2.3 and 2.4.

Applying the structure of the sol-coagulation model to the kinetic model from Section 2.3 and the growth model in Section 2.4, we attain the following equation. It is also illustrated by Figure 2.17. Let N_i be the concentration of i-mers and B_i be the concentration for bin i using the binning method previously described. We then derive the following sol-coagulation model.

$$\frac{\partial A}{\partial t} = D_A \frac{\partial^2 A}{\partial x^2} - K_1 AB \tag{2.38a}$$

$$\frac{\partial B}{\partial t} = D_B \frac{\partial^2 B}{\partial x^2} - K_1 AB \tag{2.38b}$$

$$\frac{\partial N_1}{\partial t} = D_1 \frac{\partial^2 N_1}{\partial x^2} + K_1 AB + 2K_1^- N_2 + \sum_{i=3}^{CCS} -2K_{i-1}^- N_i - 2K_1^+ N_1^2 - \sum_{i=2}^{CCS} K_i^+ N_1 N_i \tag{2.38c}$$

$$\vdots \tag{2.38d}$$

$$\frac{\partial N_i}{\partial t} = D_i \frac{\partial^2 N_i}{\partial x^2} + K_{i-1}^+ N_1 N_{i-1} + K_i^- N_{i+1} - K_i^+ N_1 N_i - K_{i-1}^- N_i \tag{2.38e}$$

$$\vdots \tag{2.38f}$$

$$\frac{\partial N_{CCS}}{\partial t} = D_{CCS} \frac{\partial^2 N_{CCS}}{\partial x^2} + K_{i-1}^+ N_1 N_{i-1} - K_{CCS}^+ N_1 N_{CCS} - K_{CCS-1}^- N_{CCS} \tag{2.38g}$$

$$\frac{\partial B_1}{\partial t} = D_{B_1} \frac{\partial^2 B_1}{\partial x^2} - \sum_{i=1}^{end-1} c(i) K_{1,i} B_1 B_i \tag{2.38h}$$
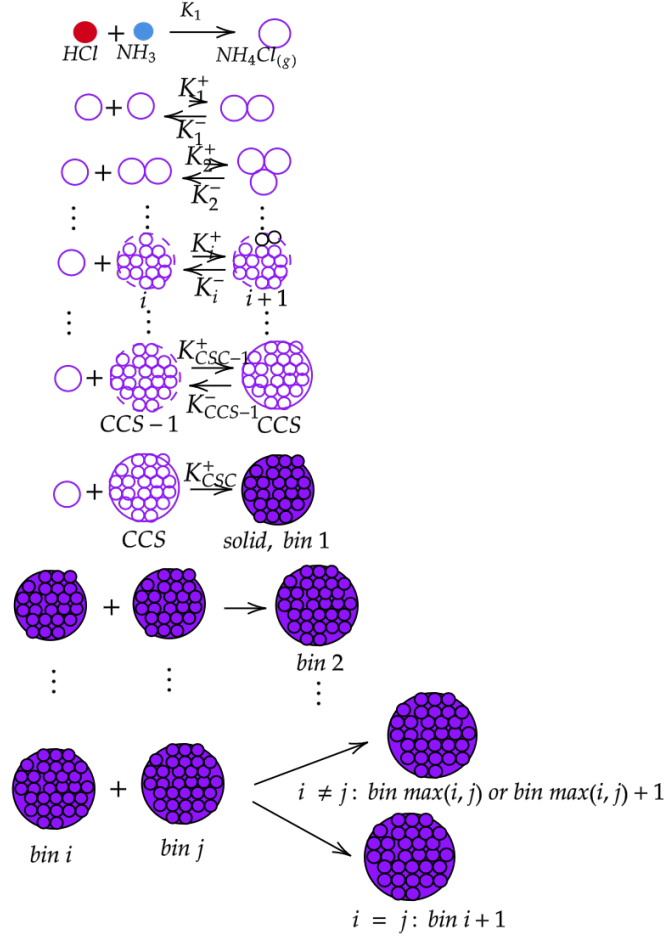
$$\vdots \tag{2.38i}$$

Figure 2.17: A visualization of the sol-coagulation model. It essentially combines the models from sections 2.3 and 2.4.

$$\frac{\partial B_k}{\partial t} = D_k \frac{\partial^2 B_k}{\partial x^2} - \sum_{i=1}^{\text{end}-1} c(i) K_{k,i} B_k B_i + \sum_{i=1}^{k} K_{k,i} B_k B_i \left(1 - \frac{m_{k,i} - m_k}{m_{k+1} - m_k}\right)$$
$$+ \sum_{i=1}^{k-1} K_{k-1,i} B_{k-1} B_i \left(\frac{m_{k-1,i} - m_{k-1}}{m_k - m_{k-1}}\right) \tag{2.38j}$$

Together, this model accounts for the formation of monomer gas, the aggregation of gas particles to form nucleated clusters, and the growth of these nucleated clusters.

The boundary conditions and initial conditions are the same as was previously used for the smaller models within this one. While this model is perhaps more thorough than others, is it also the most complicated. Using a critical cluster size of 23 for the $HCl + NH_3$ system and 36 bins for

mass doubling, there are close to 50 equations. This model is not numerically simulated here, but the goal is to someday do so. Modifications could be made to this model as well to include addition mechanisms in the aggregation of gas leading to nucleation and in the growth of nucleated particles, such as allowing monomer gas to nucleate onto precipitate, mimicking heterogeneous nucleation.

2.6   Conclusion & Future Work

This paper laid the groundwork for a variety of different models for Liesegang pattern formation and nucleation and growth as a whole. It is important to note that the models laid out here are theoretical, and the only way to test these models is to numerically compare them to observational and experimental data. This is the primary goal moving forward. The following bullet points highlight the specific work that remains for each model.

- Hashmi's function in Section 2.1 does produce Liesegang rings, but the rings do not match all of the behavior mentioned in Singh's data. If this model is modified further, a sigmodial function could be used instead of Hashmi's function so that the parameters η and ν are not necessary.

- The kinetic nucleation and growth model in Section 2.3 has the potential to produce Liesegang rings. The basic mechanism of the model using monomer growth should be re-evaluated to ensure it is physical, and if so, the correct parameters for the system need to be determined.

- The model in Section 2.4 shows promise in tracking the growth of nucleated material. Some possible modifications to the model could focus of a different binning or re-binning process and/or adding condensation to the model. This PDE also needs to be numerically simulated using a different solving method than MATLAB's pdepe. The model may also need some adjustments to allow monomer gas to nucleate into larger bins.

- If the models in Sections 2.3 and 2.4 produce accurate results that match Singh's data and observations, they can be combined into the sol-coagulation model outlined in Section 2.5.

46

Hopefully, an accurate sol-coagulation model could provide deeper insight into the true mechanics of Liesegang pattern formation and answer the question: when is the pattern actually made?

- As a whole, postnucleation models could also be incorporated into modeling to account for secondary ring growth like Singh notes in his observations. Perhaps a combination of a pre- and postnucleation model could produce accurate Liesegang patterns, as was done in [1].

- It would be interesting to expand this model to 3 dimensions. Since the tube in the experiment is so thin, it is a reasonable assumption to simplify the model to one dimension. However, in expanding to 3 dimensions we could include convection in the model, which is a process that can visually be seen influencing the reaction.

Much future work remains, but my hope is that the models outlined here lay a groundwork for advancements in understating and modeling Liesegang pattern formation.

Bibliography

[1] Maurice Chacron and Ivan L'Heureux. A new model of periodic precipitation incorporating nucleation, growth and ripening. *Physics Letters A*, 263(1-2):70–77, November 1999.

[2] Kuk Cho, Kang-Sup Chung, and Pratim Biswas. Coagulation Coefficient of Agglomerates with Different Fractal Dimensions. *Aerosol Science and Technology*, 45(6):740–743, April 2011.

[3] G. T. Dee. Patterns Produced by Precipitation at a Moving Reaction Front. *Physical Review Letters*, 57(3):275–278, July 1986. Publisher: American Physical Society.

[4] N. R. Dhar and A. C. Chatterji. Theorien der liesegangringbildung. *Kolloid-Zeitschrift*, 37(2):89–97, 1925.

[5] M. Droz, J. Magnin, and M. Zrinyi. Liesegang patterns: Studies on the width law. *The Journal of Chemical Physics*, 110(19):9618–9622, may 1999.

[6] J. M. Duley, A. C. Fowler, I. R. Moyles, and S. B. G. O'Brien. On the Keller–Rubinow model for Liesegang ring formation. *Proceedings of the Royal Society A: Mathematical, Physical and Engineering Sciences*, 473(2205):20170128, September 2017.

[7] J. M. Duley, A. C. Fowler, I. R. Moyles, and S. B. G. O'Brien. Regularization of the Ostwald supersaturation model for Liesegang bands. *Proceedings of the Royal Society A: Mathematical, Physical and Engineering Sciences*, 475(2228):20190154, August 2019.

[8] Ryan Goh, Samantha Mesuro, and Arnd Scheel. Coherent structures in reaction-diffusion models for precipitation. *Research Signpost*, pages 73–93, 2010. Publisher: Citeseer.

[9] Hamish Gordon, Jasper Kirkby, Urs Baltensperger, Federico Bianchi, Martin Breitenlechner, Joachim Curtius, Antonio Dias, Josef Dommen, Neil M. Donahue, Eimear M. Dunne, Jonathan Duplissy, Sebastian Ehrhart, Richard C. Flagan, Carla Frege, Claudia Fuchs, Armin

Hansel, Christopher R. Hoyle, Markku Kulmala, Andreas Kürten, Katrianne Lehtipalo, Vladimir Makhmutov, Ugo Molteni, Matti P. Rissanen, Yuri Stozkhov, Jasmin Tröstl, Georgios Tsagkogeorgas, Robert Wagner, Christina Williamson, Daniela Wimmer, Paul M. Winkler, Chao Yan, and Ken S. Carslaw. Causes and importance of new particle formation in the present-day and preindustrial atmospheres: CAUSES AND ROLE OF NEW PARTICLE FORMATION. *Journal of Geophysical Research: Atmospheres*, 122(16):8739–8760, August 2017.

[10] Alan Hammond. Coagulation and diffusion: A probabilistic perspective on the Smoluchowski PDE. *Probability Surveys*, 14(none), January 2017.

[11] Bahaudin Hashmi, Patrick Shipman, Jiangguo Liu, Stephen Thompson, and Ryan Goh. Mathematical modeling for liesegang rings in the vapor-to-particle reaction-diffusion system. *tbd*, in preparation.

[12] Jonathan F. Henry, Alvaro Gonzalez, and Leonard K. Peters. Dynamics of NH_4Cl Particle Nucleation and Growth at 253–296 K. *Aerosol Science and Technology*, 2(3):321–339, December 1982.

[13] Joseph B. Keller and Sol I. Rubinow. Recurrent precipitation and Liesegang rings. *The Journal of Chemical Physics*, 74(9):5000–5007, May 1981. Publisher: American Institute of Physics.

[14] Mel Edward LeVan and John Ross. Measurements and a hypothesis on periodic precipitation processes. *The Journal of Physical Chemistry*, 91(24):6300–6308, 1987.

[15] Raphael Eduard Liesegang. Ueber einige eigenschaften von gallerten. *Naturwissenschaftliche Wochenschrift*, 11:353–362, 1896.

[16] Richard Lorenz. Lehrbuch der allgemeinen Chemie, con W. Ostwald. II. Band. 2. Teil: Verwandtschaftslehre. 1. Lieferung. (Leipzig, 1896.) 5 mark. *Zeitschrift fur anorganische Chemie*, 15(1):239–239, 1897.

[17] Marcel B. J. Meinders, William Kloek, and Ton van Vliet. Effect of Surface Elasticity on Ostwald Ripening in Emulsions. *Langmuir*, 17(13):3923–3929, June 2001.

[18] Hideki Nabika, Masaki Itatani, and István Lagzi. Pattern Formation in Precipitation Reactions: The Liesegang Phenomenon. *Langmuir*, 36(2):481–497, January 2020. Publisher: American Chemical Society.

[19] Wilhem Ostwald. Ein Wort der Mathematik an die Energetik. *Annalen der Physik und Chemie*, 293(1):39–71, 1896.

[20] Eli Ruckenstein and Gersh Berim. *Kinetic theory of nucleation*. Chapman and Hall/CRC, 2016.

[21] S. Sadek and Rabih Sultan. Liesegang patterns in nature: A diverse scenery across the sciences, a review paper. *Precipitation Patterns in Reaction-Diffusion Systems*, pages 1–43, 01 2011.

[22] John H. Seinfeld and Spyros N. Pandis. *Atmospheric chemistry and physics: from air pollution to climate change*. J. Wiley, Hoboken, N.J, 2nd ed edition, 2006. OCLC: ocm62493628.

[23] Swaren Singh. *Diffusion and Reaction in the Ammonia-Hydrogenchloride System*. PhD thesis, The University of Manchester Institute of Science of Technology, October 1968.

[24] M. V. Smoluchowski. Drei Vortrage uber Diffusion, Brownsche Bewegung und Koagulation von Kolloidteilchen. *Zeitschrift fur Physik*, 17:557–585, January 1916.

[25] Tharwat Tadros. *Kelvin Equation*, pages 679–680. Springer Berlin Heidelberg, Berlin, Heidelberg, 2013.

[26] Stephen Thompson and Patrick D. Shipman. Patterns, Oscillations, and Microtornadoes: Extreme Events in Vapor-to-particle Reaction Zones. *Procedia IUTAM*, 9:138–164, 2013.

[27] Stephen Thompson, Patrick D. Shipman, Stephen P. Shipman, and Todd J. Zurlinden. The counterdiffusion of HCl and NH_3: An experimental and modeling analysis of topochemistry,

diffusion, reaction, and phase transitions. *The Journal of Chemical Physics*, 150(15):154306, April 2019.

[28] Hui Zhang, Kan Zhan, Yulu Chen, Guoxia Chen, Xiaomei Zhou, Junxiu Liu, Min Wu, and Henmei Ni. Three dimension Liesegang rings of calcium hydrophosphate in gelatin. *Journal of Sol-Gel Science and Technology*, 71, 09 2014.